Trigger Algorithms and Monte Carlo Event Generation for Dijet Searches in ATLAS and Beyond

Master's Thesis in Physics

by

Sebastian Murk

December 19, 2016

Department für Physik
Friedrich-Alexander-Universität Erlangen-Nürnberg

LUND UNIVERSITY
Faculty of Science

Division of Particle Physics
Department of Physics
Lund University

Supervisor: Dr. Caterina Doglioni

Originality Statement

This is to certify that the results presented in this thesis represent my own work and have not been previously submitted for a degree or diploma at any other institution of higher education. I furthermore certify that, to the best of my knowledge, my thesis does not infringe upon anyone's copyright nor violate any proprietary rights. Any material - including figures and tables - that has been previously published or written by another author is clearly marked as such. No resources other than the ones referenced have been used in the preparation of this thesis.

Sebastian Murk

_____

Signature

_____

Date

Acknowledgements

My time at Lund University has been truly magnificent, not least because of the many wonderful people I got to work with. It is here that I want to show my appreciation for your help and support. It goes without saying that this cannot be done without the extensive use of cheesy particle physics anecdotes ;)

To Caterina:
Thank you for your sound advice and continuous support over the course of my thesis. You have been an outstanding mentor. Despite your busy schedule, you always made time when the situation required it. You have taught me a lot about QCD and jets, but beyond that, I like to believe you have also taught me a lot about academic life in general :) Also, I have to admit that I am a bit envious of your ability to multi-task: it is nothing short of admirable; in fact, one might even say it is unprecedented, much like the record-setting luminosity recorded by ATLAS this year ;)

To my gluon octet (Edgar, Eric, Eva, Juno, Katja, Prim, Trine, Will):
Thank you for making my life at LU more colourful ;) it would have been much more dull without the presence of each and everyone of you, as my past summer-self can assure you. I will certainly miss the many shared lunches, dinners, fikas(!!), and nights out. I wish all of you the best of luck for your current and future endeavours!

To Torbjörn:
Thank you for your elucidations regarding the inner workings of `PYTHIA`. Thanks to your calm and patient demeanour, I always enjoyed learning from you :)

To Torsten, Else and Oxana:
All of you have had a hand in the planning and organisation of my studies at Lund University in one way or another. As a matter of fact, it was the three of you (and Caterina) with whom I first exchanged emails prior to coming to Sweden. Thank you for your support and for giving me the opportunity to come to Lund!

Last but not least, I would like to thank all members of the Lund particle physics division; everyone of you has helped make the past year one to remember. Tack så jättemycket!

Preliminary Remarks

Acronyms
An alphabetically sorted list of acronyms that are used throughout the thesis is provided on pages x-xi. Bold print is used to indicate acronym formation.

Bibliography Entries
If an article lists more than five contributing authors without specifying a lead author, either the name of the collaboration (if applicable) or the first name according to alphabetical order followed by "et al." will be quoted. If an article has appeared in one or multiple journals, the name(s) of the journal(s) will be referenced in the article's bibliography entry. If an article has not been published in a journal (regardless of whether or not it has been submitted to one or multiple journals), the institution and department of the leading author(s) at the time of the article's completion are quoted instead of the journal's name.

Feynman Diagrams
Feynman graphs were created with the *TikZ-Feynman* package in LaTeX [1]. Unless specified otherwise, the convention used in this thesis is to have the time axis run from left to right. Incoming (outgoing) particle states are placed on the left (right) side of the graph.

Figures and Tables
Figures and tables that have not been created by myself contain a reference to their origin in the figure/table caption. This is also true for tables that have been created by myself but make use of numerical values that have been extracted from an external resource. Table entries "-" indicate that a column/row is not applicable to an entry or that no reliable resource has been found to extract a numerical value.

Notation and Units
Bold print is used rather than elevated arrows to indicate vector quantities such as particle momenta, e.g. $\boldsymbol{p}$ is used instead of $\vec{p}$. Unless specified otherwise, natural units ($c = \hbar = 1$) are used throughout the thesis.

Public Code
`C++` and `Python` code created over the course of this thesis is publicly available at https://github.com/murksebastian/MScThesis-MCpythiaDijet.

Abstract

Despite its success in describing non-gravitational interactions, many of the theoretical and experimental shortcomings of the SM remain unresolved. In collider searches, **B**eyond the **S**tandard **M**odel (BSM) signatures are expected to manifest themselves as localised excesses of events in the invariant mass lineshape of their decay products. Alternatively, they may become apparent as deviations in the observed shape of angular distributions. In order to discern BSM phenomena, the expected SM background has to predicted with very high accuracy. This is achieved by use of **M**onte **C**arlo (MC) techniques.

The ATLAS dijet **T**rigger **L**evel **A**nalysis (TLA) searches for processes indicative of new physics in final states comprising two jets. Due to the large SM multijet background and the limited bandwidth available to inclusive single-jet triggers, the low mass regime of this search signature is not well constrained by previous experiments. To alleviate the bandwidth limitation, a 20 GeV minimum threshold for the jet transverse momentum has been implemented to reduce the average event size, thus allowing to record events at a higher rate and ultimately resulting in an increased search sensitivity.

In the second part of this thesis, kinematic and angular distributions of dijet topologies are studied using the MC event generator `PYTHIA 8.219`, including topologies with an additional associated jet that have not been considered in previous MC studies. Pure dijet topologies are corrected up to **N**ext-to-**L**eading **O**rder (NLO) using k-factors derived from the **M**atrix **E**lement (ME) event generator `NLOJET++`. Topologies with associated jet production are studied using a reweighting procedure to account for the reduced strong interaction scale associated with the emission of soft jets, as well as under variation of the minimum angular separation between two jets.

Table of Contents

List of Tables

List of Figures

List of Acronyms

ATLAS **A** **T**oroidal **L**HC **A**pparatu**s**.

BSM **B**eyond the **S**tandard **M**odel.

CDF **C**ollider **D**etector at **F**ermilab.

CERN European Organisation for Nuclear Research (adapted from the original French title "**C**onseil **E**uropéen pour la **R**echerche **N**ucléaire").

CM **C**entre-of-**M**ass.

CMS **C**ompact **M**uon **S**olenoid.

DM **D**ark **M**atter.

DS **D**ata **S**couting.

DSP **D**ark **S**ector **P**article.

ECal **E**lectromagnetic **Cal**orimeter.

EF **E**vent **F**ilter.

EMEC **E**lectro**M**agnetic **E**nd-**C**ap.

EW **E**lectro**W**eak.

EWSB **E**lectro**W**eak **S**ymmetry **B**reaking.

FCal **F**orward **Cal**orimeter.

FSR **F**inal **S**tate **R**adiation.

HCal **H**adronic **Cal**orimeter.

HEC **H**adronic **E**nd-**C**ap.

HLT **H**igh **L**evel **T**rigger.

ID **I**nner **D**etector.

ISR **I**nitial **S**tate **R**adiation.

L1 **L**evel-**1**.

L2 **L**evel-**2**.

LAr **L**iquid **Ar**gon.

LHC **L**arge **H**adron **C**ollider.

LHCb **L**arge **H**adron **C**ollider **b**eauty.

LO **L**eading **O**rder.

LS1 **L**ong **S**hutdown **1**.

MC **M**onte **C**arlo.

ME **M**atrix **E**lement.

MS **M**uon **S**pectrometer.

NLO **N**ext-to-**L**eading **O**rder.

NNLO **N**ext-to-**N**ext-to-**L**eading **O**rder.

PDF **P**arton **D**istribution **F**unction.

PS **P**arton **S**hower.

QCD **Q**uantum **C**hromo**D**ynamics.

QED **Q**uantum **E**lectro**D**ynamics.

QFT **Q**uantum **F**ield **T**heory.

RoI **R**egion **o**f **I**nterest.

SM **S**tandard **M**odel.

SNR **S**ignal-to-**N**oise **R**atio.

SSB **S**pontaneous **S**ymmetry **B**reaking.

TLA **T**rigger **L**evel **A**nalysis.

Chapter 1

Introduction

The **S**tandard **M**odel (SM) of particle physics [2, 3, 4] (Section 2.1) is the most successful theory of elementary particles to date. Its accuracy in describing physical phenomena is unparalleled, and its predictions have been verified in numerous experiments. Nevertheless, it is incomplete. In particular, recent astronomical observations suggest the existence of forms of matter that are not contained within the SM, most notably **D**ark **M**atter (DM) [5] and dark energy [6]. If so-called Dark Sector Particles (DSPs) [7] interact non-gravitationally with SM particles, they can be produced in high energy particle collisions and identified via their decay signatures. More specifically, they will become apparent as resonances ("bumps") in the invariant mass spectrum.

The ATLAS experiment (Chapter 3) is designed to be sensitive to a wide range of physics, including new phenomena that reach **B**eyond the **S**tandard **M**odel (BSM), e.g. the previously mentioned resonances caused by DM mediators. It is used to study the outcomes of high energy proton-proton collisions delivered by the CERN **L**arge **H**adron **C**ollider (LHC), the most powerful particle accelerator ever built. Due to the large **Q**uantum **C**hromo**D**ynamics (QCD) (Section 2.2) cross sections, high momentum physics at the LHC is dominated by so-called jets (Section 4.1), making search signatures comprising final state jets all the more challenging in view of the overwhelming background and limited bandwidth.

This thesis describes the search for new resonances in the ATLAS dijet **T**rigger **L**evel **A**nalysis (TLA) (Chapter 4), specifically the implementation of a 20 GeV **H**igh **L**evel **T**rigger (HLT) cut placed on the jet transverse momentum that significantly reduces the average event size. In combination with the newly developed **D**ata **S**couting (DS) technique (Section 4.3), this allows for a sensitivity increase in the search for low mass dijet resonances, a domain that is not well constrained by previous experiments.

To identify processes indicative of BSM physics, the SM background expectation has to be predicted with high accuracy. This is achieved by use of **M**onte **C**arlo (MC) techniques (Section 5.1). In this thesis, both kinematic variables (Section 5.4) and angular distributions (Section 5.5) are examined using the MC event generator `PYTHIA`

8.219 [8, 9]. Throughout these studies, pure dijet topologies are compared with topologies comprising an additional associated jet. For the latter, the results presented in this thesis are the first results available of a detailed MC study using PYTHIA 8.219.

Chapter 2

Theoretical Framework

This chapter summarises the mathematical and conceptual foundations underlying the studies presented in this thesis. Section 2.1 is a brief overview of the **S**tandard **M**odel (SM) of particle physics [10]. Due to its key role in the formation of jets, the theory of **Q**uantum **C**hromo**D**ynamics (QCD) is discussed in greater detail in Section 2.2. Lastly, the concept of *Feynman diagrams* is introduced (Section 2.3).

2.1 The Standard Model of Particle Physics

The culmination of theoretical particle physics is called the **S**tandard **M**odel of particle physics, or simply **S**tandard **M**odel. It strives to describe nature in terms of fundamental particles and the interactions between them. The term "fundamental" (or "elementary") reflects the belief that these particles are not composed of smaller, primary constituents; they are truly fundamental (to the best of our current knowledge). As illustrated in Figure 2.1, fundamental particles can be categorised according to their intrinsic properties such as electric charge, colour charge, and spin.

A first distinction is made between force mediating particles (spin-1 gauge bosons) and particles that make up matter, i.e. quarks and leptons[1]. The latter come in six flavours that can be arranged in three generations of self-contained doublets:

$$\textit{quark doublets:} \quad \begin{bmatrix} u \\ d \end{bmatrix} \quad \begin{bmatrix} c \\ s \end{bmatrix} \quad \begin{bmatrix} t \\ b \end{bmatrix}$$

$$\textit{lepton doublets:} \quad \begin{bmatrix} e \\ \nu_e \end{bmatrix} \quad \begin{bmatrix} \mu \\ \nu_\mu \end{bmatrix} \quad \begin{bmatrix} \tau \\ \nu_\tau \end{bmatrix}$$

It should be noted that only the first generation (shaded grey in Figure 2.1) is needed to make up ordinary matter. The second and third generations can be thought of as heavier, less stable duplicates of the first. They emerge from high energy collisions such as those produced in particle colliders and cosmic rays.

[1] Due to their spin-½ nature, quarks and leptons may be referred to collectively as fermions.

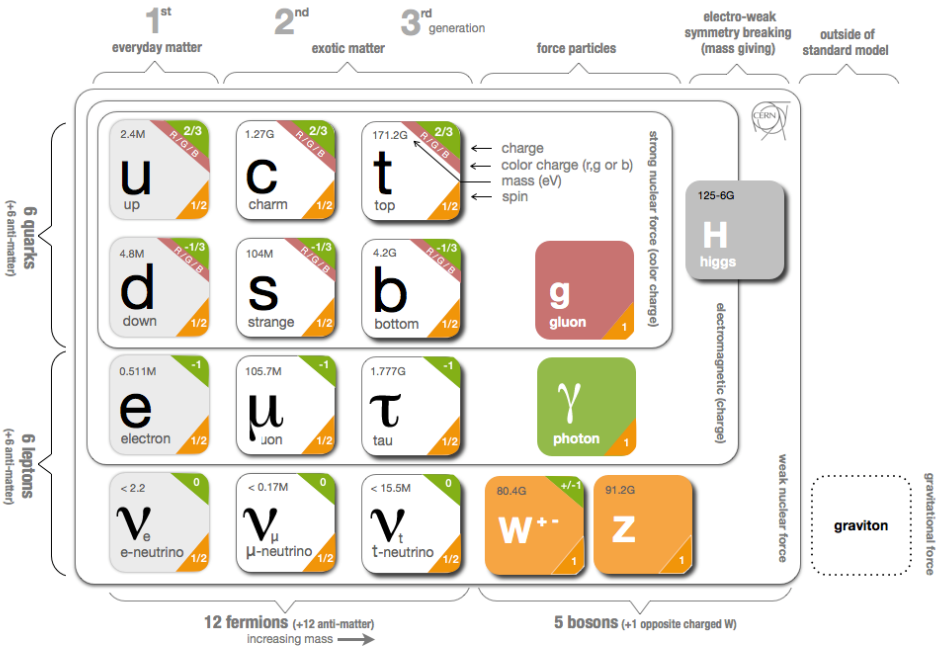

Figure 2.1: Classification scheme for fundamental particles [11].

The mathematical formalism of the SM is a renormalisable, relativistic **Q**uantum **F**ield **T**heory (QFT) with local gauge invariance[2] based on the gauge group [4]

$$\mathcal{G}_{\mathrm{SM}} = \mathcal{SU}(3)_C \otimes \mathcal{SU}(2)_L \otimes \mathcal{U}(1)_{Y_w} \ , \tag{2.1}$$

where $\mathcal{U}(n)$, $\mathcal{SU}(n)$ denote *unitary* and *special unitary groups* of order $n \in \mathbb{N}$, respectively. It incorporates three of the four fundamental forces of nature: electromagnetism, the weak interaction, and the strong interaction. Each of them is associated with one or multiple force mediating spin-1 gauge bosons. More precisely, the number of force mediating bosons associated with an interaction is given by the dimension of its conjugate *Lie Group*. For a *special unitary group* $\mathcal{SU}(n)$ of order n, the dimension is given by $n^2 - 1$. For a *unitary group* $\mathcal{U}(n)$ of order n, it is simply n^2 [13]. The colour symmetry group $\mathcal{SU}(3)_C$ for instance is of order three and represents the strong interaction. It is mediated by eight distinct types of gluons commonly referred to as *colour octet*. The physical quantity conserved in all strong interactions is the colour charge as is indicated by the subscript $_C$. It can take on three discrete values commonly denoted red(r), green(g), and blue(b), along with their corresponding anticolours antired($\bar{r}$), antigreen($\bar{g}$), and antiblue($\bar{b}$). Anticolours are carried only by antiquarks and vice versa. Leptons do not carry any colour charge and thus cannot interact with each other via the exchange of

[2]Simply put, this implies that the action $\mathcal{S} = \int L \, dt$ is left invariant, i.e. remains unchanged, under transformations of the form $\mathcal{A}^\mu \to \mathcal{A}'^\mu = \mathcal{A}^\mu + \partial^\mu \chi$ for a given potential A^μ and an arbitrary function $\chi(x^\mu)$ [12].

gluons. This is visualised in Figure 2.1 by the black contour encircling the six flavours of quarks and the force mediating gluon(s). In an analogous manner, black contours are used to illustrate the fermion couplings to the gauge bosons of the electromagnetic and weak interaction.

Electromagnetism and the weak interaction are two manifestations of the same force that are only distinguishable at relatively low energies. Above the aptly named ***E**lectro**W**eak unification energy* ($\approx$ 246 GeV [14]), they are embodied by the expression $\mathcal{SU}(2)_L \otimes \mathcal{U}(1)_{Y_w}$ [15] as a unified description of electromagnetism and the weak interaction. Here, the subscript $_L$ is used to indicate that $\mathcal{SU}(2)_L$ couples only to left-handed fermion (and right-handed antifermion) chiralities[3] [2].

The physical quantity that governs a particle's behaviour in weak interactions is (the third component of) its *weak isospin* T_3. Analogous to colour and electric charge, it reverses sign for antiparticles ("charge conjugation"). While all particles of left-handed chirality have a weak isospin of $\pm$½, all particles of right-handed chirality have a weak isopsin of zero and therefore do not participate in weak interactions [16]. The generator Y_w of the $\mathcal{U}(1)_{Y_w}$ group is called *weak hypercharge* and relates a particle's electric charge Q and its weak isospin T_3 [2]:

$$Y_w = 2\,(Q - T_3) \tag{2.2}$$

Weak hypercharge and weak isospin are conserved in all particle interactions.

The three mediators of the weak interaction are Z^0, W^+ and W^-. Unlike all other force carriers, the charged W bosons couple to fermion pairs that differ in charge by ± 1 and thus possess the unique ability to change the flavour of fermions with which they interact. This property and its ramifications are of great importance. One of the most prominent examples is radioactive decay, as depicted in Figure 2.2. Since this type of interaction requires a transfer of electric charge at the vertex, the W boson coupling is said to be associated with a *weak flavour-changing charged current* [4]. Since no charge is transferred in interactions that involve the electrically neutral Z^0 boson, the Z^0 is said to be associated with a *neutral current*.

The $\mathcal{SU}(2)_L \otimes \mathcal{U}(1)_{Y_w}$ subgroup predicts four massless force carrying gauge bosons, whereas experimental values are as high as 80.4 GeV/c^2 for the $W^\pm$ and 91.2 GeV/c^2 for the Z^0 boson [17, 18]. For a long time, this conundrum was puzzling both experimentalists and theorists alike. It was resolved by the discovery that below the EW unification energy, the full EW gauge group $\mathcal{SU}(2)_L \otimes \mathcal{U}(1)_{Y_w}$ is broken down to an exact $\mathcal{U}(1)_{QED}$ symmetry via **S**pontaneous **S**ymmetry **B**reaking (SSB) (in this context often also referred to as **E**lectro**W**eak **S**ymmetry **B**reaking (EWSB) or "Higgs mechanism"), i.e. [16, 19]

[3] Introducing the notion of *handedness*, *helicity* and *chirality* with all of its subtleties is beyond the scope of this thesis. A rather comprehensive description is provided in [3].

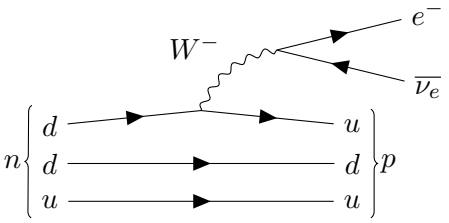

Figure 2.2: Conversion of a down quark into an up quark in nuclear β^- decay: $n \to p + e^- + \overline{\nu_e}$.

$$\mathcal{G}_{\mathrm{SM}} = \mathcal{SU}(3)_C \otimes \mathcal{SU}(2)_L \otimes \mathcal{U}(1)_{Y_w} \xrightarrow{EWSB} \mathcal{SU}(3)_C \otimes \mathcal{U}(1)_{QED} \,. \tag{2.3}$$

It can be derived mathematically that EWSB requires the presence of a complex scalar doublet field $\phi \in \mathbb{C}^2$ ("Higgs field") that permeates all space [20]. An excitation of such a field is detectable as a scalar (spin-0) particle: the Higgs boson [21, 22]. It is the only scalar boson in the **S**tandard **M**odel (SM) and furthermore the only SM particle that had not been observed prior to the start-up of the LHC.

The fourth fundamental force - gravity - is not included in the SM and its corresponding hypothesised mediator - the graviton - has not yet been observed. It is postulated to emerge as a massless spin-2 boson [4, 23]. A comparison of the four fundamental interactions is provided in Table 2.1.

interaction	*mediator*	*couples to*	*rel. strength*	*range*
Strong	gluon (g)	colour charge C	1	10^{-15} m
Electromagnetism	photon (γ)	electric charge Q	10^{-2}	∞ ($\propto r^{-2}$)
Weak	$W^{\pm}$, Z^0	weak isospin T_3	10^{-5}	10^{-18} m
Gravitation	graviton (G)	mass m	10^{-39}	∞ ($\propto r^{-2}$)

Table 2.1: Juxtaposition of the four fundamental interactions. Coupling strengths[4] have been normalised with respect to the strong interaction [4].

2.2 Quantum Chromodynamics

The study of $\mathcal{SU}(3)_C$ interactions is dubbed **Q**uantum **C**hromo**D**ynamics (QCD) [2, 4] based on the Greek word for colour, "chroma". Even though the concept of colour is by no means related to actual visible colours in this context, the name is quite well chosen due to a peculiar property of QCD known as *colour confinement.* It states that "solitary" quarks cannot exist. Instead, they must unite to form composite, colour neutral ("white") particles. Colour neutrality can be achieved in two ways: by "mixing"

[4]The listed values are approximated and serve only as a coarse comparison. The true values of the coupling constants are not fixed and depend on the energy scale (or, equivalently, the length scale) that is considered. Hence, they are often referred to as "running coupling constants".

all of the three (anti)colours together or by adding a colour to its corresponding anticolour. The resulting bound particles are fermionic three quark states (qqq or $\bar{q}\bar{q}\bar{q}$) called *(anti)baryons* and bosonic quark-antiquark states ($q\bar{q}$) called *mesons*[5]. Altogether, composite particles consisting of quarks and/or antiquarks are referred to as *hadrons*[6].

The earliest experimental indication for the existence of colour dates back to the observation of the first pion nucleon $\pi^+ p$ resonance Δ^{++} with charge $Q = 2$ and spin $J = \frac{3}{2}$ in 1951 [27, 28], a configuration that correctly matches the properties of a bound uuu baryon state. Since quarks are fermions, this state would violate the *Pauli exclusion principle*[7] if it were not for the presence of an additional quantum number: the colour charge.

In contrast to **Q**uantum **E**lectro**D**ynamics (QED) - the description of electromagnetic interactions characterised by the exchange of photons - QCD is *non-Abelian*. This implies an important qualitative difference: whereas photons themselves do not carry any electric charge, gluons do carry (anti)colour charges and thus interact among themselves[8]. The various independent linear superpositions of colour and anticolour charges constitute the eight gluon colour states represented in the $\mathcal{SU}(3)_C$ colour octet. Similar to how the $W^\pm$ bosons of the weak interaction can change the flavour of a fermion with electric charge, gluons can change the colour (but not the flavour!) of a quark.

The self-coupling capability of gluons has profound implications that become apparent when the impact of *charge screening* in QED is compared against the same effect in QCD, cf. Figure 2.3. The screening process relies heavily on the production of virtual particles made possible by the uncertainty inherent in quantum mechanics[9]. In QED, for instance, an electron e^- may spontaneously emit a virtual photon. The virtual photon can subsequently annihilate to produce a virtual electron-positron $e^- e^+$ pair, and so forth, see Figure 2.3 (top left). Ultimately, the original electron is surrounded by a cloud of virtual $e^- e^+$ charges that - due to the attractive (repulsive) force exerted on the positrons (electrons) according to *Coulomb's law* - will arrange themselves such that the positrons are located closer to the initial electron, thus effectively forming a polarised medium ("vacuum polarisation"). In consideration of these circumstances, it is clear that the observed charge depends on the distance at which the electron is probed. Due to the

[5] The term antimeson can be misleading and is seldom used, since both mesons and antimesons each consist of one quark and one antiquark; in an antimeson, quarks are simply replaced by their corresponding (i.e. same flavour) antiquarks and vice versa.

[6] Just recently, evidence for the existence of four [24, 25] and five [26] quark states (so-called "tetra-" and "pentaquarks") has been presented by the LHCb Collaboration. They are sometimes referred to as *exotic hadrons*.

[7] The *Pauli exclusion principle* states that within a quantum system, a quantum state cannot be occupied by more than one fermion simultaneously. In other words, fermion states that form part of the same quantum system have to differ in at least one quantum number.

[8] The same applies to the gauge bosons of the weak interaction, since $\mathcal{SU}(2)_L$ is also *non-Abelian*.

[9] According to *Heisenberg's uncertainty principle* [29], the conservation of energy can be violated for a time period $\Delta t < \hbar/\Delta E$, where ΔE denotes the energy required for the classically forbidden process. Alternatively, one could interpret virtual particles as particles that do not satisfy the relativistic energy-momentum relation, i.e. $p^2 = E^2 - \boldsymbol{p}^2 \neq m^2$, where p^2 denotes the square of the four-momentum.

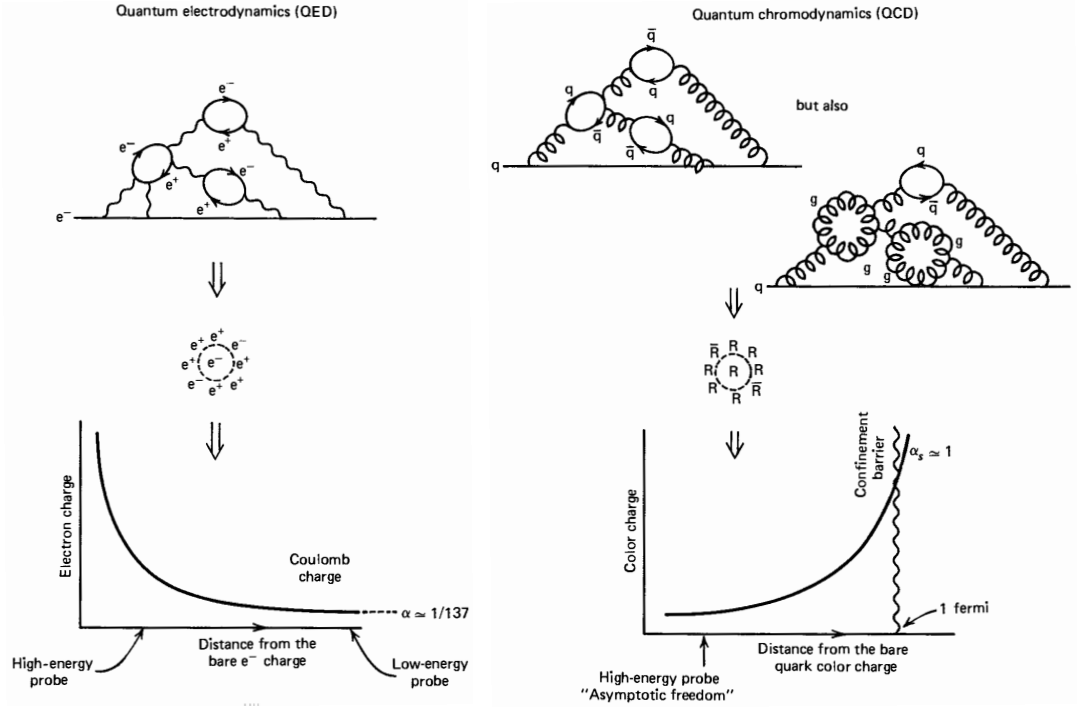

Figure 2.3: Charge screening in QED (left) vs. charge screening in QCD (right) [2].

screen provided by the positrons, the charge that is observed becomes asymptotically smaller as the distance increases, cf. Figure 2.3 (bottom left). Conversely, as one moves closer to the electron, penetrating the polarised cloud of virtual particles, the observed charge increases. As a matter of fact, the running coupling that has been alluded to in Section 2.1 can be attributed to precisely this phenomenon: Since the coupling strength α_{em} of the electromagnetic interaction is proportional to the square of the electric charge, i.e. $\alpha_{\text{em}} \propto e^2$, the impact of *charge screening* in QED is to reduce the coupling strength for long distance (or, equivalently, low energy) interactions. For historical reasons, the constant value $\alpha_{\text{em}} \simeq 1/137$ that is approached in the limit of infinitely large distances is known as *fine structure constant*.

In principle, the screening mechanism in QCD works in much the same manner. However, since gluons couple not only to quarks, but also to each other, new configurations involving pure gluon-gluon vertices have to be considered in addition to quark-gluon vertices, see Figure 2.3 (top right). While the influence of virtual $q\bar{q}$ pairs (*quark polarisation*) is analogous to virtual e^-e^+ pairs in QED, the impact of virtual gluons (*gluon polarisation*) is exactly opposite and reverses the familiar result of QED[10]. The net impact of *charge screening* in QCD can be deduced from the critical parameter[11] [3, 30]

[10] This behaviour is not obvious a priori. For a detailed derivation, the reader is referred to [30].

[11] Note that this is a simplified expression. Strictly speaking, one would have to consider that a) $n_F = 6$ is only true if enough energy is available to "access" all six flavours of quarks, i.e. $> m_{\text{top}} \approx 173$ GeV [18],

$$\beta_0 = 11 n_C - 2 n_F \ , \tag{2.4}$$

where n_C (n_F) denotes the number of colours (flavours) and $\beta_0 < 0$ corresponds to an increase of the coupling strength at short distances (as in QED). In QCD, $n_C = 3$, $n_F = 6$, and hence $\beta_0 > 0$ (*anti-screening*), which implies that the coupling strength α_s of the strong interaction decreases as the distance is shortened (corresponding to high energies / large momenta), cf. Figure 2.3 (bottom right). As a consequence, quarks inside *hadrons* behave as essentially free, non-interacting particles. This property, referred to as *asymptotic freedom*, is unique to the strong interaction.

On the other hand, the potential energy $V(r)$ between two quarks grows roughly linearly as the separation r between them increases [4]:

$$V(r) = -\frac{4}{3}\frac{\alpha_s}{r} + kr \tag{2.5}$$

At a certain distance, it becomes energetically favourable to create a real (as opposed to virtual) $q\bar{q}$ pair from the vacuum in order to break the long-range force. This process, known as *fragmentation*, is the physical mechanism concealed within the abstract notion of *colour confinement*. As will become apparent in Chapter 4, *fragmentation*[12] and *asymptotic freedom* play a crucial role in the formation of jets.

The running coupling constant α_s of the strong interaction can be expressed as a function of the momentum transfer Q squared, i.e. (at lowest order) [30]

$$\alpha_s(Q^2) = \frac{12\pi}{\beta_0 \ln\left(Q^2/\Lambda^2_{QCD}\right)} \quad , \tag{2.6}$$

where the *confinement scale parameter* Λ_{QCD} corresponds roughly to the energy boundary between asymptotically free quarks ($Q \gg \Lambda_{QCD}$) and quarks confined in *hadrons* ($Q \lesssim \Lambda_{QCD}$). Measurements of Λ_{QCD} typically yield a value between 100 MeV and 500 MeV [4].

2.3 Feynman Diagrams

Particle interactions can be depicted by so-called *Feynman diagrams*[13] [4], see Figure 2.4. Apart from serving as a means of illustration, they are of pivotal importance for the computation of measurable physical quantities such as *cross sections*, from which *decay rates* and *probabilities* for the occurrence of a particular process can be derived. In a *Feynman diagram*, every line and every vertex corresponds to a mathematical term in the calculation. In particular, each vertex contributes a factor proportional to $\sqrt{\alpha}$ (with α

and b) the n_F factor depends on charge, i.e. quarks of different flavours will contribute in different amounts.

[12] often used interchangeably with the term *hadronisation*, esp. in the context of jet formation

[13] named after Nobel laureate Richard Feynman (1918-1988)

the coupling strength; cf. Figure 2.4) to the *Lorentz invariant amplitude* $\mathcal{M}_{fi}$ connecting the initial and final state particles. Calculations keeping only the first order coupling term in the series expansion for $\mathcal{M}_{fi}$ are referred to as **L**eading **O**rder (LO) calculations. Those keeping higher order coupling terms are labelled successively as **N**ext-to-**L**eading **O**rder (NLO), **N**ext-to-**N**ext-to-**L**eading **O**rder (NNLO), and so forth.

Note that an exact calculation would require the summation over the contributions of an infinite series of diagrams with a continuously growing number of vertices and loops. Of course, this is not feasible in practice. Fortunately, however, higher-order diagrams can be neglected as their contributions become vanishingly small very rapidly in the realm of small running coupling constants, i.e. in the low energy regime of QED and the high energy regime of QCD (cf. Figure 2.3 (bottom half)). This idea is at the heart of *perturbation theory*. It often allows to obtain precise predictions of physical observables using only a few low order diagrams. On the other hand, calculations involving sizeable running coupling constants do not allow to make predictions with arbitrary precision and are called *non-perturbative*.

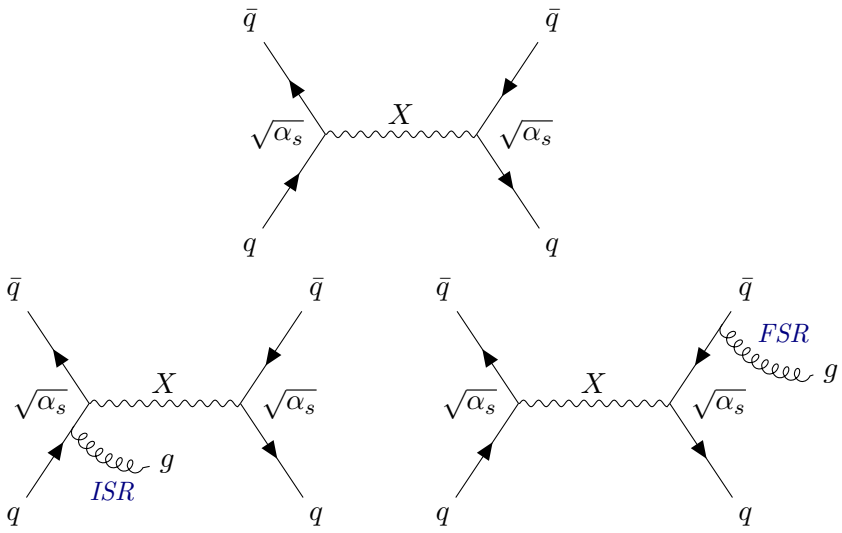

Figure 2.4: LO Feynman graphs for the production of a new light resonance X decaying to pairs of jets with and without (top) recoil against an **I**nitial **S**tate **R**adiation (ISR) (bottom left) and **F**inal **S**tate **R**adiation (FSR) (bottom right) jet.

Chapter 3

The ATLAS Experiment

In this chapter, the ATLAS experiment [31] at the CERN **L**arge **H**adron **C**ollider is introduced [10]. A truly international endeavour, the ATLAS collaboration comprises roughly 3000 scientists from over 175 institutions in 38 member states. For brevity, priority is given to detector components of high relevance for the work presented in this thesis, i.e. the ATLAS calorimeter and trigger system. A description of the ATLAS **I**nner **D**etector (ID), **M**uon **S**pectrometer (MS) and magnet system is not provided in this thesis. For an in-depth review of the ATLAS detector, the reader is referred to [32].

3.1 The Large Hadron Collider

Situated in Geneva, Switzerland, the **L**arge **H**adron **C**ollider (LHC) operated by CERN is currently the most powerful high energy particle accelerator in the world [33]. With a **C**entre-of-**M**ass (CM) energy of $\sqrt{s} = 13$ TeV and a record-setting peak luminosity[1] of $\mathcal{L} = 1.37 \cdot 10^{34}\ \mathrm{cm}^{-2}\,\mathrm{s}^{-1}$ [35] in Run 2, it is one of the most advanced experimental tools for probing SM predictions, and its potential for discoveries indicative of new physics is far beyond any of its predecessor experiments.

3.2 The ATLAS Detector

ATLAS - **A** **T**oroidal **L**HC **A**pparatu**s** - is one of two general-purpose detectors[2] at the LHC used to investigate a wide range of physics. It exhibits a forward-backward symmetric cylindrical geometry and is aligned concentrically around the LHC beam pipe. With dimensions of 44 m × 25 m (height × diameter), it is one of the largest volume

[1] Not to be confused with the astrophysical quantity of the same name. In particle physics, the luminosity $\mathcal{L}$ is a measure of the performance of a particle collider. It is proportional to the collision rate and often quoted in terms of integrated luminosity $\mathcal{L}_{\mathrm{int}} = \int \mathcal{L}(t)\, dt$, i.e. luminosity accumulated over time [34].

[2] The second detector is operated by the CMS collaboration [36]. Even though both experiments pursue the same scientific goals, they are led independently and exploit distinct technical solutions in their detectors, e.g. different magnet system designs. Aside from eliminating the risk of erroneous discoveries due to faulty detector components, this approach also allows for cross-confirmation in the case of a new discovery, as has been the case in the aforementioned Higgs boson discovery in 2012 [21, 22].

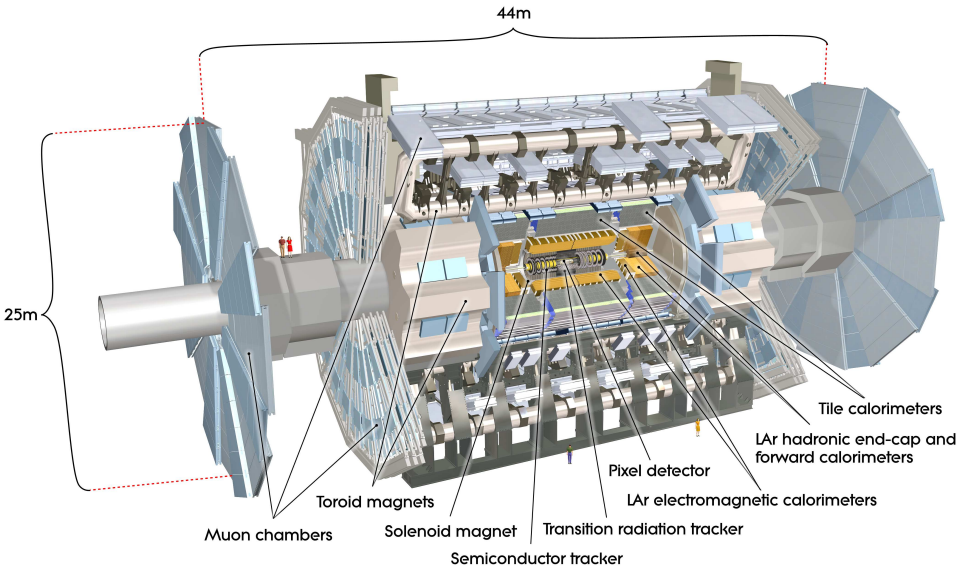

Figure 3.1: Cut-away view of the ATLAS detector [32].

particle detectors that has ever been built. Figure 3.1 shows an overview of the ATLAS detector and its main components. As can be seen, it comprises a toroidal magnet system and several detector subsystems, each of them designed to perform a specific task such as particle identification, tracking, energy measurement, etc. Figure 3.2 demonstrates - layer by layer - what particle types the various detector subcomponents are sensitive to. Neglecting detector inefficiencies, every SM particle passing through the detector - except for neutrinos - will yield a signal.

3.2.1 Coordinate Convention

It is common practice in particle physics to work with a coordinate system that is tailored to the geometry of the detector, which - in the case of ATLAS (and CMS) - exhibits cylindrical symmetry. The ATLAS collaboration uses a right-handed coordinate system in which the beam direction defines the z-axis, cf. Figure 3.3. The origin coincides with the centre of the detector and is referred to as interaction point. The positive x-axis is defined as pointing from the interaction point to the centre of the LHC ring, and the positive y-axis as pointing upward. Since the x-y-plane is transverse to the beam axis z, it is referred to as *transverse plane*. Observables measured in the transverse plane are labelled with the subscript $_T$, i.e. E_T and p_T for transverse energy and momentum, respectively. It is often more convenient to use *polar coordinates* (r, ϕ) to label points in the transverse plane, where $r = \sqrt{x^2 + y^2}$ denotes the radius and $\phi \in [0, 2\pi]$ the *azimuthal angle* around the z-axis defined from the positive x-axis. When using spherical coordinates (r, ϕ, θ), the *polar angle* $\theta \in [0, \pi]$ is defined from the positive y-axis. Consequently, all physical quantities measured in the transverse plane can be expressed as a function of θ. A particle's transverse momentum p_T, for instance, may be written as $p_T = p \sin\theta$.

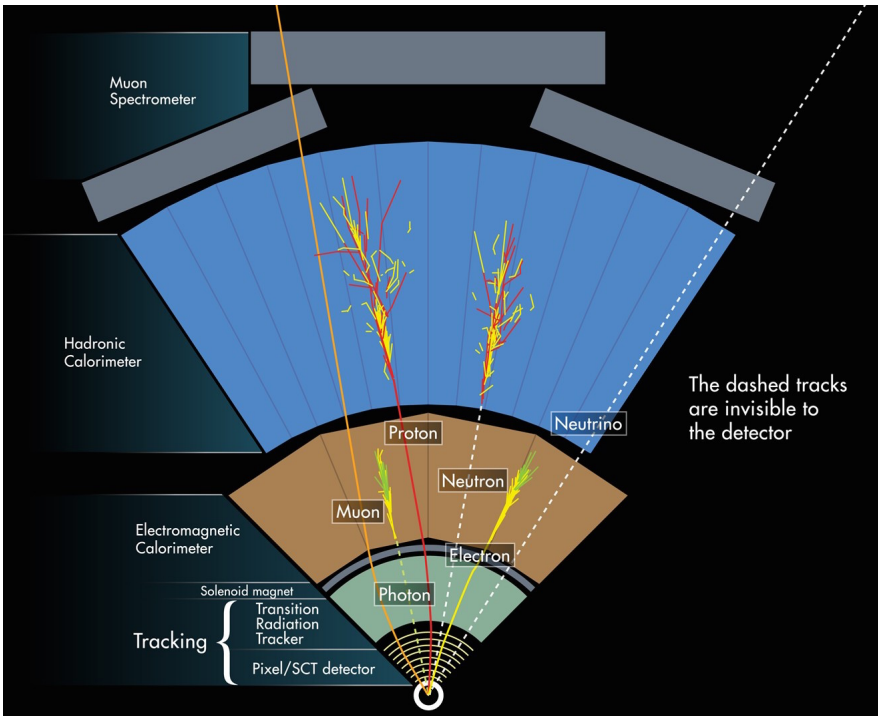

Figure 3.2: Schematic diagram illustrating the identification of different types of particles based on their interactions with the ATLAS detector [37].

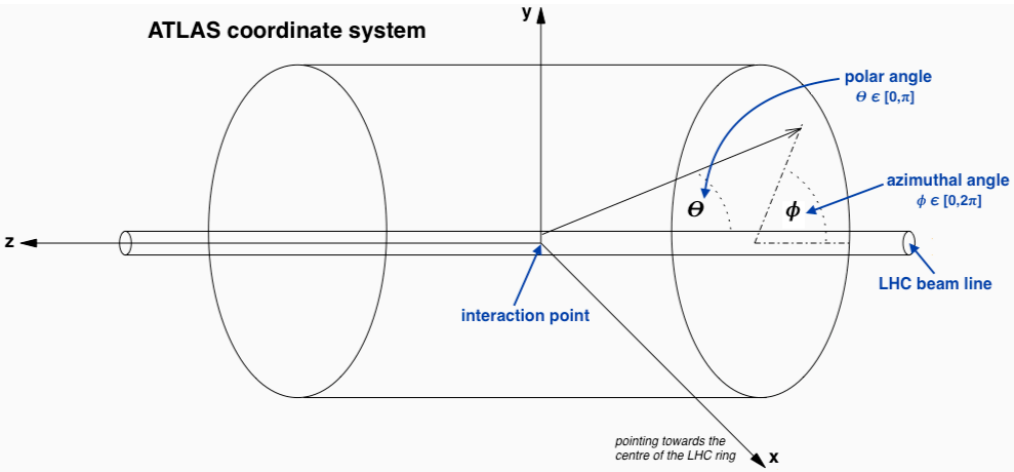

Figure 3.3: Schematic representation of the ATLAS coordinate system, adapted from [38].

Having introduced the *polar angle* θ, it is useful to define the *pseudorapidity*

$$\eta := -\ln\left[\tan\left(\frac{\theta}{2}\right)\right] \ . \tag{3.1}$$

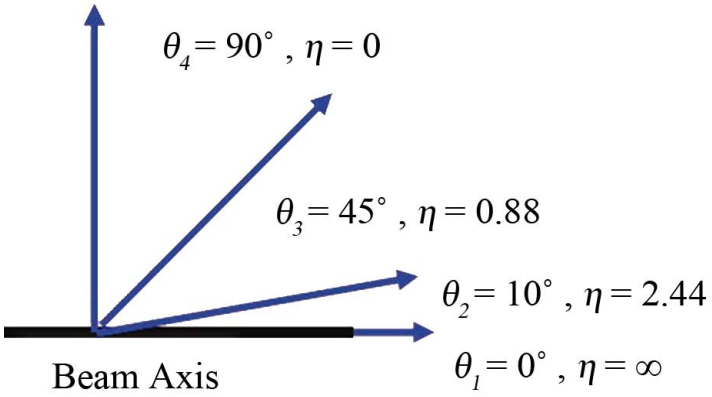

Figure 3.4: Illustration of the pseudorapidity η, adapted from [39].

As illustrated in Figure 3.4, it is a quantitative measure of a particle's angle relative to the beam axis z. It is commonly used to specify the angular range that certain detector components are sensitive to, see Section 3.2.2.

3.2.2 Calorimetry

The ATLAS calorimeter system consists of the **E**lectromagnetic **Cal**orimeter (ECal), the **H**adronic **Cal**orimeter (HCal) and the **F**orward **Cal**orimeter (FCal), see Figure 3.5. Its primary objective is to measure the energy and position of electrons, photons (ECal and FCal) and hadrons (HCal and FCal) [20]. Calorimeters are also sensitive to electrically neutral particles, e.g. neutrons or neutral mesons, as they give rise to secondary particles via inelastic scattering processes. Based on their distinct interactions with the detector, it is possible to distinguish electrons and photons from pions and muons, for example. Moreover, calorimeters allow for indirect detection of neutrinos and other invisible particles through measurement of an event's missing transverse energy[3] E_T^{miss} (cf. Section 3.2.1). Calorimeters deployed in the ATLAS detector are sampling calorimeters with ϕ-symmetry and complete and uniform coverage around the beam axis[4] [32]. A sampling calorimeter is composed of alternating layers of a dense material to absorb incident particles and an active material to produce an output signal that is proportional to

[3] Conservation of momentum in the transverse plane implies that the vectorial sum over all transverse momenta equals zero in the absence of undetectable particles such as neutrinos and many BSM hypotheticals (neglecting inaccuracies in the measurements). The *missing transverse momentum* [14] is defined as two-dimensional vector in the transverse plane, and its absolute value is commonly referred to as *missing transverse energy* $E_T^{\text{miss}} = \left(E_x^{\text{miss}}, E_y^{\text{miss}}\right)$, where $E_i^{\text{miss}} = \sum E_i^{\text{miss},\alpha}$ and $E_i^{\text{miss},\alpha} = -\sum p_i^{\alpha}$, with $i \in \{x, y\}$ and $\alpha \in \{e, \gamma, \tau, \text{jets}, \mu, \text{soft}\}$.

[4] However, one should keep in mind that as time progresses, a few calorimeter modules will fail to work correctly due to e.g. radiation damage and/or electrical faults.

the energy of the incident particle[5] [41]. Table 3.1 summarises the η coverage of individual calorimeter components. Combined, ECal, HCal and FCal cover the pseudorapidity range $|\eta| < 4.9$ [32]. For brevity, the FCal will not be discussed in this thesis.

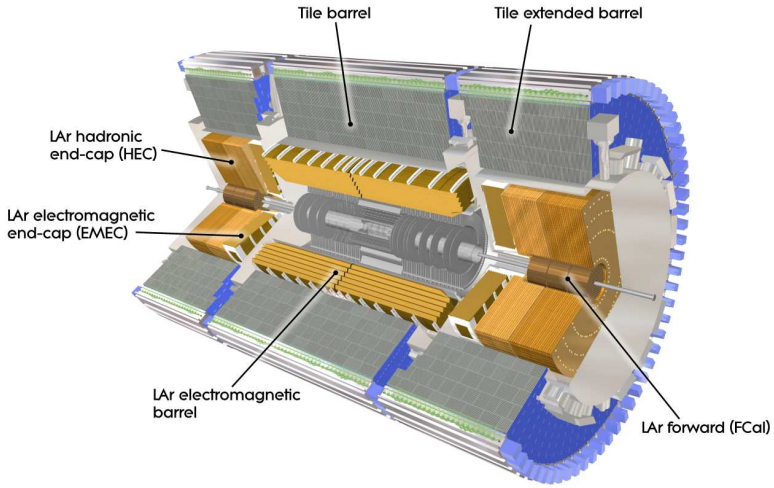

Figure 3.5: Cut-away view of the ATLAS calorimeter system [32].

Calorimeter Element	η Coverage	Rad. Lengths [X_0]	Int. Lengths [λ]
LAr ECal barrel	$\lvert\eta\rvert < 1.475$	> 22	-
LAr EMECs	$1.375 < \lvert\eta\rvert < 3.2$	> 24	-
HCal tile barrel	$\lvert\eta\rvert < 1.0$	-	≈ 9.7
HCal extended tile barrel	$0.8 < \lvert\eta\rvert < 1.7$	-	≈ 9.7
LAr HECs	$1.5 < \lvert\eta\rvert < 3.2$	-	≈ 10

Table 3.1: Pseudorapidity coverage and total thickness in terms of radiation lengths (X_0) or interaction lengths (λ) of the ATLAS calorimeters [32].

Above approximately 1 GeV, electrons and photons produce secondary photons via bremsstrahlung and secondary electrons and positrons via pair production in photon-photon collisions ($\gamma + \gamma \rightarrow e^+ + e^-$), respectively. The result is a cascade of particles ("particle shower") with progressively diminishing energies (illustrated in Figure 3.2). At energies below 1 GeV, particles from the shower ionise atoms in the **L**iquid **Ar**gon (LAr) layers. The ions can then be collected and converted into a signal that is proportional to the energy of the incident particle.

[5] In contrast, homogeneous calorimeters are built of only one type of material that performs both tasks. A comprehensive summary of different calorimeter types - including their assets and drawbacks - is given in [40].

3.2.2.1 Electromagnetic Calorimeter

The ECal uses lead absorber plates and LAr as an active medium. It comprises the LAr electromagnetic barrel and two LAr **E**lectro**M**agnetic **E**nd-**C**aps (EMECs). An accordion geometry is used for the absorbers and electrodes of the ECal barrel and end-caps to reduce detector response time. A fast signal response time ($\mathcal{O}(50$ ns)) is needed to meet the operating requirements at the high collision frequencies of the **L**arge **H**adron **C**ollider (LHC). In a classical calorimeter, the ionisation signal produced by particle showers is collected by electrodes located in the middle of the LAr layers, whereas in the accordion-shaped ECal, the signal is extracted directly from the front and back faces of the calorimeter. This minimises the amount of capacitance and inductance inducing cables, thereby reducing the overall response time. See Figure 3.6 for a comparison of ordinary and accordion calorimeter geometry.

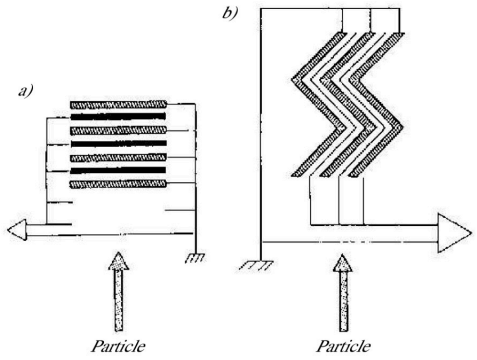

Figure 3.6: Traditional a) and accordion b) calorimeter geometry [40].

3.2.2.2 Hadronic Calorimeter

The HCal is designed specifically to measure the energy of hadrons. It consists of one tile-shaped barrel, two extended tile barrels and two LAr **H**adronic **E**nd-**C**aps (HECs). Analogous to the EMECs, the HECs are LAr sampling calorimeters using copper plates as absorber material. They are each composed of two consecutive wheels placed orthogonal to the beam axis with an absorber thickness of 25 and 50 mm, respectively [42]. The hadronic tile calorimeters are sampling calorimeters using scintillating[6] tiles as the active material and iron as the absorber. The scintillating tiles are made of a fluorescent material. In contrast to LAr calorimeters, where the signal yield is proportional to the amount of charge collected by the electrodes, the signal strength picked up by the tiles is proportional to the amount of light, i.e. the number of photons and their respective energies. A calorimeter of this type is referred to as scintillator calorimeter. Both sides of the scintillating tiles are read out by wavelength shifting fibres into two separate photomultipliers [43].

[6] When struck by a charged particle or high-energy photon, the energy is absorbed and re-emitted it in the form of photons ("scintillation").

3.2.3 Trigger System

The storage capacity and data collection bandwidth of ATLAS is significantly smaller than the overwhelming rate of collisions delivered by the LHC. Besides, BSM processes are generally predicted to occur very rarely, i.e. at minute rates compared to the total inelastic pp cross section. A dedicated real-time filter system that allows to select interesting events against the very large backgrounds without bias is therefore crucial to the success of searches for BSM physics. The event selection is based on telltale detector signatures, such as the presence of objects with high transverse momentum p_T (e.g. jets, cf. Section 4.1) or missing transverse energy E_T^{miss}. The ATLAS Run 2 trigger system consists of two components: A **L**evel-**1** (L1) hardware trigger and a software-based **H**igh **L**evel **T**rigger (HLT).

3.2.3.1 Level-1 Trigger

The L1 trigger uses a subset of coarse detector information from the calorimeters and **M**uon **S**pectrometer to identify so-called **R**egions **o**f **I**nterest (RoI) based on features readily available during early reconstruction. At this stage of the event selection, jets are identified with a sliding window algorithm described in more detail in Section 4.2.1. To keep the latency at a minimum, the L1 trigger operates using custom-made readout electronics with mostly hardwired logic. Despite the fact that the decision time allocated to this first stage of the event selection is less than 2.5 µs, a strong reduction from the 40 MHz bunch-crossing rate (at a bunch-spacing of 25 ns) to an event rate of 100 kHz is achieved [44]. RoI are passed on to the HLT, where higher resolution detector information is made available to reduce the even rate further.

3.2.3.2 High Level Trigger

Because it is preceded by the **L**evel-**1** (L1) trigger, more computing time is available in the second stage of event selection. In consequence, the HLT uses more refined selection algorithms to examine RoI at full detector granularity including tracking and topological information, similar to offline reconstruction techniques [45]. Jets are identified using the anti-k_t algorithm outlined in Section 4.2.2. On average, the rate of events that pass the HLT and are recorded for offline processing is 1 kHz [44].

Chapter 4

Search for Low Mass Dijet Resonances with the ATLAS Trigger Level Analysis

In this chapter, the search strategy of the ATLAS dijet TLA[1] is outlined. Some general information about searches for BSM phenomena with jets is provided in Section 4.1. A concise overview of trigger jet algorithms used in Run 2 of the LHC is given in Section 4.2. The newly developed **D**ata **S**couting (DS) technique is discussed in conjunction with the significance of the 20 GeV jet-p_T trigger threshold in Section 4.3.

4.1 Jet Searches in ATLAS

Jets are narrowly collimated clusters of (mostly hadronic) particles that form via successive *hadronisation* (cf. Section 2.2) of highly relativistic *partons*[2] that emerge from the collisions in the LHC. Since each *hadronisation* process is initiated by a single high momentum quark (or gluon), the collimated shape of jets can be deduced as a direct consequence of momentum conservation. Any new resonance produced at a hadron collider, i.e. via coupling to initial state partons (cf. Figure 2.4), can certainly decay back into jets, whereas coupling to leptons is not a prerequisite for the production of a new resonance. Together with the fact that they are the most common high-p_T ("hard") objects produced at the LHC [46], this makes jets very effective experimental tools in the search for new physics phenomena[3].

Collider searches for DSPs examine the invariant mass line shape for anomalies in the observed event yields corresponding to a new resonance. If such a resonance exists, it will manifest itself as a significant positive deviation from the expected SM background, i.e. a localised excess of events. As will become clear in Section 5.5, differences predicted in the shape of angular distributions will be more pronounced for narrow resonances[4].

[1] A TLA uses physical objects (jets in the case of the dijet TLA) that are reconstructed by the trigger reconstruction software as opposed to fully reconstructed offline analyses.
[2] The term *parton* is used as a common handle for the constituents of *hadrons*, i.e. quarks and gluons.
[3] However, note that jets, if not used as part of the search signature, often make for dominant contributions to the background of many SM and BSM analyses.
[4] Also, note that the resonance width $\Gamma = \hbar/\tau$, i.e. the parameter that defines exactly how localised

Search signatures containing final state jet pairs (cf. Figure 2.4) are particularly intriguing in the low mass regime, where large gaps remain uncovered by previously conducted experiments, especially in the realm of small vector couplings g_B to quarks[5], see Figure 4.1. As indicated (black circle), a comparatively large area in the M_{Z_B}-g_B-plane is currently not constrained by previous experiments. In fact, the best limits currently available for masses below approximately 650 GeV date back to results obtained by the CDF collaboration [47], see Figure 4.1. This search domain is targeted by the ATLAS dijet TLA discussed in what follows.

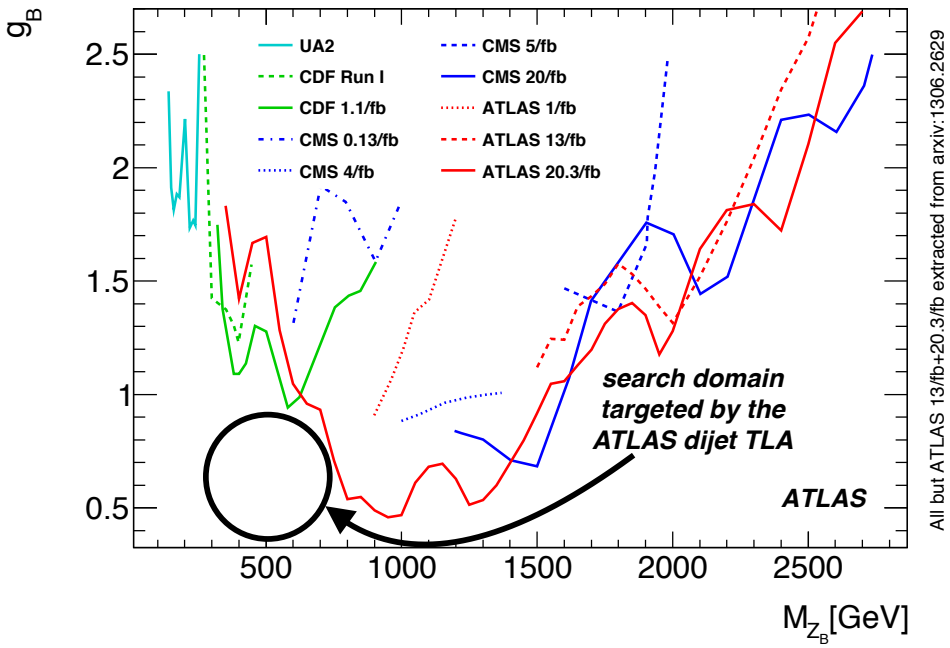

Figure 4.1: Summary of the currently available upper limits on the vector coupling g_B of a new leptophobic dijet resonance M_{Z_B} from different experiments, incl. results from Run 1 of the LHC at $\sqrt{s}$ = 7-8 TeV (red lines); adapted from [48].

4.2 Jet Trigger Algorithms

4.2.1 Trigger Towers and Sliding Window Algorithm

At the L1 trigger stage, a *sliding window algorithm* [45, 49] using so-called *trigger towers* as input is used for jet finding. The algorithm works as follows: The calorimeter system

an observed excess of events is, is inversely proportional to the lifetime τ of the new particle, that is $\Gamma \propto \tau^{-1}$.

[5] Recall Chapter 2: The coupling strength g of a vector mediator determines how strongly it interacts with SM fermions. In this case, the new mediator is assumed to be *leptophobic*, meaning that it will only couple to quarks.

(cf. Section 3.2.2) is divided into cells of size $\Delta\eta \times \Delta\phi = 0.2 \times 0.2$ in η-ϕ-space (cf. Section 3.2.1). In the case of a high energy event, the accumulated energy of all cells in a longitudinal layer is summed into the so-called *trigger tower energy*. Then, a window of fixed size $N_\eta \times N_\phi$ is moved across the calorimeter cell grid in steps of $\Delta\eta$ and $\Delta\phi$. If the transverse energy contained within a window (≡ sum of transverse energies of all towers located within the window boundaries) is above the trigger threshold and corresponds to a local maximum, a jet precluster is formed. The window size as well as the trigger threshold are optimised so as to limit the rate of fake preclusters caused by detector noise while retaining a good efficiency for jet (precluster) finding. Interesting regions (RoI) are then passed on to the HLT for further analysis.

4.2.2 Topological Clusters and Anti-k_T Algorithm

As outlined in the previous section, jet inputs are identified by means of energy deposits in the ATLAS calorimeter system. At the HLT, this is done using a *clustering algorithm* [49], i.e. one that makes use of geometrical detector information to reconstruct the spatial distribution of energy in three dimensions: If adjacent calorimeter cells register energy deposits that are well above the expected noise level, they are grouped into topological clusters ("topoclusters") according to the *4-2-0 scheme* [49, 50], see Figure 4.2: First, a *topocluster* is seeded by an individual cell if $S/N \geq 4\sigma$, i.e. if the **S**ignal-to-**N**oise **R**atio (SNR) is greater than or equal to four times the standard deviation of the observed noise distribution. The cluster grows via iterative addition of neighbouring cells, provided they satisfy $S/N \geq 2\sigma$. In a final step, all remaining adjacent cells are included. Note that topoclusters comprise a variable number of cells, unlike the fixed-size preclusters formed by the sliding window algorithm discussed in Section 4.2.1. Topoclusters are used as input for the so-called *anti-k_t* algorithm [52]. Denoting the distance between two physical objects (e.g. particles, jets) d_{ij} and the distance of an object to the beam d_{iB}, one can define the measures

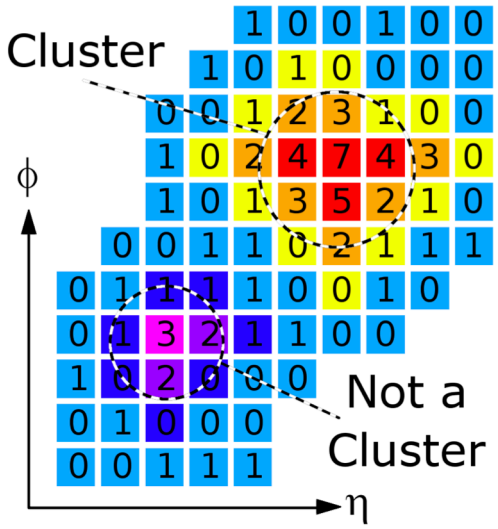

Figure 4.2: Pictorial representation of the ATLAS clustering algorithm in two dimensions. Numerical values correspond to the energy deposited in the cell divided by its Gaussian width σ_{noise} (measured in randomly triggered events) [51].

$$d_{ij} = \min\left(k_{ti}^{2p}, k_{tj}^{2p}\right)\frac{\Delta_{ij}^2}{R^2} \quad , \quad \Delta_{ij} := (y_i - y_j)^2 + (\phi_i - \phi_j)^2 \ , \tag{4.1}$$

$$d_{iB} = k_{ti}^{2p} \qquad \text{with} \quad p = -1 \quad \text{for the anti-}k_t\text{ algorithm} \ , \tag{4.2}$$

where k_{ti}, y_i, ϕ_i denote respectively the transverse momentum, rapidity and azimuthal angle of object i, and R the radius of the jet cone. The *anti-k_t* algorithm works as follows:

1. evaluate both distance measures:
   a) if $d_{ij} < d_{iB}$, recombine objects i and j
   b) if $d_{ij} > d_{iB}$, identify i as jet and remove it from the list of objects
2. recalculate distances and repeat procedure until the list of objects is empty.

4.3 Data Scouting and p_T Threshold

Searches for light dijet resonances are compromised by the finite bandwidth[6] made available to *inclusive single-jet triggers* [48], i.e. any configuration of particle states may emerge alongside the jet that sets off the trigger. Consequently, the sensitivity of these searches is typically limited by the available statistics rather than systematic uncertainties, contrary to dijet searches conducted in the high mass regime. Unfortunately, operating conditions in Run 2 of the LHC are considerably more demanding on the ATLAS trigger system on account of the higher luminosity and increase in CM energy (cf. Section 3.1). Indeed, while the total rate of events recorded for physics analyses increases only by roughly a factor of two and a half, jet rates are approximately five times higher with respect to Run 1 [46]. In order to cope with the increased rates, major upgrades have been implemented during the **L**ong **S**hutdown **1** (LS1). Most importantly, the **L**evel-**2** (L2) trigger and **E**vent **F**ilter (EF), two formerly separate entities used in Run 1 of the LHC, have been merged into a single software-based **H**igh **L**evel **T**rigger (HLT) to allow for dynamic resource sharing: This implies that algorithms run in the same computing nodes, thus minimising the need for data transfers from detector buffers while increasing the algorithm flexibility at the same time [45]. In addition, the acceptance rate for events that are output by the L1 hardware trigger has been improved from 70 kHz ($\equiv$ 100 GB/s) in Run 1 to 100 kHz ($\equiv$ 160 GB/s) in Run 2 [46].

Despite the technical advances, the jet rate is too large to record all events. Therefore, it is necessary to rethink the data collection strategy in order to be able to successfully conduct a search for light dijet resonances with sub-TeV masses. Due to the large SM multijet background, full events containing the complete set of detector information can only be recorded at a manageable rate if triggers are *prescaled*. This means that only a fraction of full events is recorded and assigned a larger relative weight so as to compensate for the reduced event rate. However, this implies that the statistical significance is strongly diminished at lower dijet invariant masses as rare, interesting events are discarded at random. To circumvent this limitation, the ATLAS dijet TLA employs a so-called **D**ata **S**couting (DS) technique: The rationale is to reduce the average event size by recording merely a small subset of each event ("partial event") containing

[6] bandwidth: the transmission capacity of a computer network or other telecommunication system.

only the data that is needed for the search[7], thus allowing to record events at a much higher rate as compared to using prescaled triggers without overstraining the available trigger bandwidth at the higher collision energy of Run 2. This is illustrated in Figure 4.3.

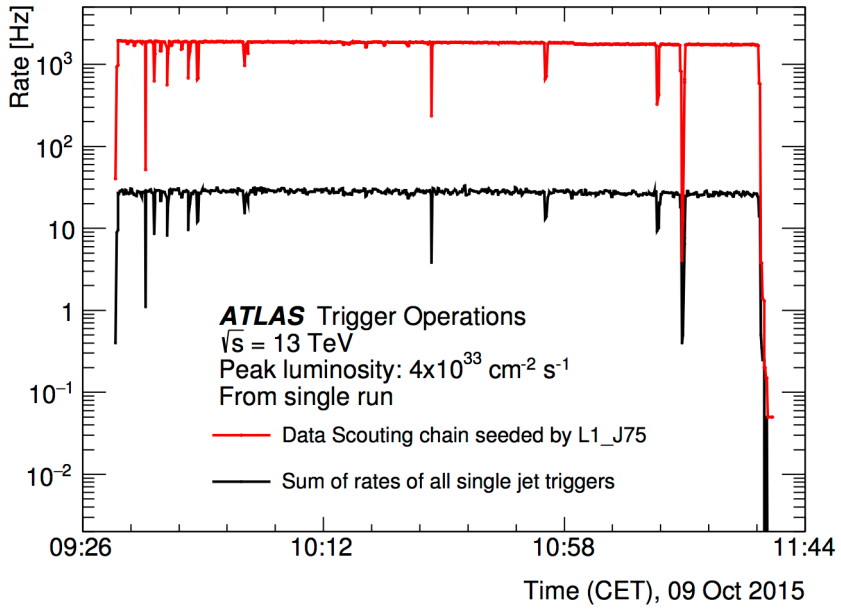

Figure 4.3: Comparison of the sum of the rates of all single jet prescaled triggers to the trigger rate of the DS chain seeded by the L1 trigger `L1_J75`. Overlaps in the rate of the single jet triggers are considered negligible [48].

The DS approach was used for the first time during the second data taking period of Run 2 that commenced in April 2016 [35]: The average size of an event containing all jets with transverse momentum above 4 GeV was only 30 kB/event [48]. While this is already an impressive improvement with regard to the 1.6 MB of a complete event containing all available detector readouts [46], it can be reduced even further to merely 10 kB/event by placing a cut of 20 GeV on the transverse momentum p_T of all HLT jet objects saved to data storage, i.e. by discarding all jets with $p_T < 20$ GeV, see Figure 4.4.

The difference in the rate of recorded events can be estimated according to Figure 4.3:

$$\Delta\nu = 2 \cdot 10^3 \text{ Hz} - 3 \cdot 10 \text{ Hz} = 1970 \text{ Hz} = 1.97 \text{ kHz} \,. \tag{4.3}$$

Since, on average, 20 kB/event are saved on account of the 20 GeV jet-p_T threshold, the total bandwidth saved per second is

$$\Delta\nu \cdot 20 \text{ kB/event} = 39400 \text{ kB/s} = 39.4 \text{ MB/s} \,. \tag{4.4}$$

[7]Since the only background to this search stems from QCD processes, it suffices to store the jet four-vectors (cf. Section 5.2, Equation (5.1)) and very few additional variables.

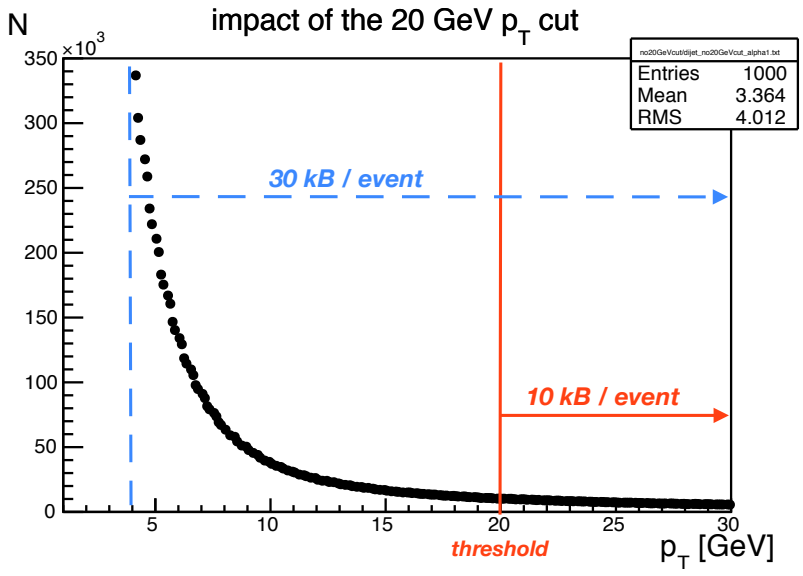

Figure 4.4: Impact of the 20 GeV minimum p_T threshold illustrated by means of a dedicated `PYTHIA` MC sample comprising one million events.

The reason that such an enormous amount of bandwidth can be saved by the comparatively simple means of a 20 GeV cut on the jet-p_T is that the p_T distribution of jets is steeply falling [50]: Low-p_T ("soft") jets are much more common than high-p_T ("hard") jets. The specification of a jet-p_T threshold therefore causes many soft objects to be rejected. This is illustrated in Figure 4.4. Nevertheless, it should be noted that it comes entirely free of adverse effects for the dijet TLA, since only the high-p_T objects are interesting for physics analysis.

Two software classes are particularly important to record events from the raw data stream, namely `TrigHLTDSSelector` and `ScoutingStreamWriter` [48]. As the name implies, the former allows to retrieve the jet collection from a chosen HLT chain, discard all jets that do not satisfy the requirement set for the minimum jet-p_T, and return the new, truncated jet collection, which is then written to bytestream by the latter. The implementation of the software-based HLT p_T threshold was one of the main objectives of this thesis and included an overhaul of some of the already existing code in the `TrigHLTDSSelector` class. In particular, the previous logic was flawed in the sense that the p_T cut was applied before the event selection took place. This is problematic for two reasons: Firstly, applying the cut beforehand may bias the event selection procedure since some objects (i.e. those with $p_T < 20$ GeV) are rejected before the event is assessed as a whole. Secondly, applying the cut after and only if an event has passed all selection requirements is much more efficient in terms of computing resources and time, two features that are crucial for the functionality of jet triggers. After initial tests in cosmic

runs[8] had turned out positive, the revised HLT code was successfully put into operation in the 2016 data taking period of Run 2 of the LHC.

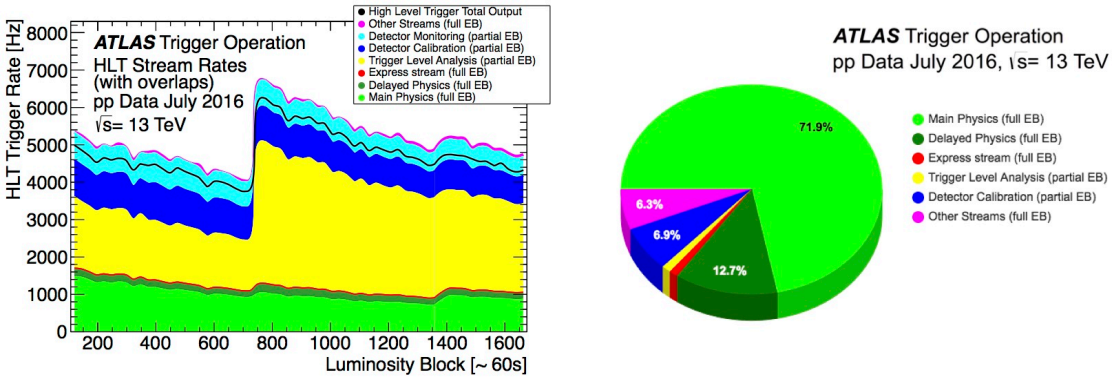

Figure 4.5: *Left:* total and individual stream rates at the ATLAS HLT as a function of luminosity blocks. *Right:* total output bandwidth of various analysis streams [53].

As illustrated in Figure 4.5, the bandwidth allocated to the ATLAS dijet TLA is tiny in comparison with the total output bandwidth at the HLT (right). In contrast, the individual TLA stream rate accounts for a large fraction of the overall stream rate (left). All stream rates decay exponentially as a result of decreasing luminosity during an LHC fill. The rate increase at luminosity block $\approx$ #720 is attributable to prescales applied in order to optimise the bandwidth usage. Small dips and peaks are caused by detector deadtime and noise, respectively [48].

One of the prerequisites for the implementation of the DS technique is that the dijet TLA can be performed with less information and fewer physical objects than what is available in a standard ATLAS event. To make use of data from the DS stream, the performance of jets reconstructed at the trigger level must be comparable to that of jets reconstructed offline. This includes jet identification, calibration and corresponding estimation of jet fake rates, energy scale resolution and uncertainties. The former was briefly discussed in Section 4.2. However, an in-depth discussion of the remaining steps in the analysis is beyond the scope of this thesis. For the full documentation on the implementation of DS in the ATLAS dijet TLA, the reader is referred to [48, 54].

[8] Runs in which all detector components are active to detect and measure cosmic particles in the absence of *pp* beams circulating and colliding in the LHC.

Chapter 5

Monte Carlo Event Generation for ATLAS Dijet Searches

This chapter presents a **M**onte **C**arlo (MC) study of kinematic and angular distributions of dijet final state topologies and their results. Section 5.1 is a short elaboration outlining the functional principles of MC event generators. The physical observables of interest are introduced in Section 5.2. Section 5.3 briefly discusses the kinematic selection implemented in the `Slowjet` algorithm, as well as the phase space cuts that have been applied. The results obtained for the kinematic variables, i.e. invariant mass m_{inv} and transverse momentum p_T, are presented and discussed in Section 5.4. Similarly, the angular variables y, y_B, $y^\star$ and (normalised) angular distributions $\frac{1}{N}\frac{dN}{d\chi}$ vs. χ are the subject of Section 5.5.

5.1 Monte Carlo Generators

MC event generators [55, 56, 57, 58] are essential components in the preparation, realisation and analysis of particle physics experiments. In particular, they are used to generate events for physics processes of interest, thereby allowing to estimate event rates before the actual experiment is conducted. This is particularly crucial in the context of BSM searches, namely to create signal and background models that allow to quantify the significance of a (hypothetical) new resonance and discern what type of particle the resonance corresponds to.

A distinction is made between two (to some extent) complementary methods, namely the ***P**arton **S**hower (PS)* and the ***M**atrix **E**lement (ME) approach* [55]: Generally, PS programs model all stages of the event generation (see below) using LO MEs (e.g. $2 \to 2$ processes with optional ISR and FSR), whereas only the hard scatter cross section is computed using exact higher order MEs in the latter. The former are thus suitable tools for developing signal and background models in the context of BSM searches. On the other hand, ME programs are better suited for high-precision measurements, but they need to be corrected for non-perturbative effects to be comparable to measurements. It goes without saying that the distinction is not always obvious, nor even applicable.

POWHEG [59, 60, 61], for instance, allows to merge higher order calculations with the PS approach. Also, neither of these approaches includes the simulation of particle interactions with the detector material. This is usually done using specialised software, such as GEANT4 [62, 63, 64].

The results presented in this thesis were generated with PYTHIA 8.219 [8, 9], a complete MC event generator with LO MEs based on the *Lund string model*[1] [65]. In the following paragraph, the event generation strategy of a PS type MC event generator (e.g. PYTHIA) is outlined, since this what is used throughout the thesis. Although some details differ, many of the generic features are common to most current general purpose event generators.

Most event generators divide the structure of a *pp* collision at the LHC into the following stages, see Figure 5.1:

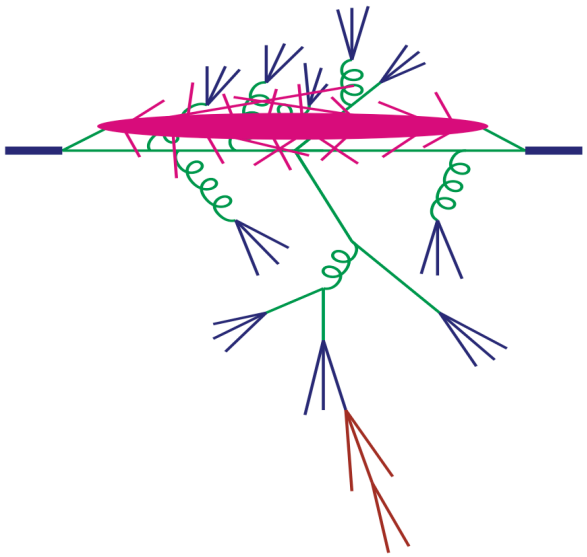

Figure 5.1: Schematic illustration of the structure of a *pp* collision at the LHC. Different colours indicate different stages in the event generation [56].

[1] hard process
Since only a small fraction of events contain a high momentum transfer process of interest, it is more efficient to start the simulation from a selected hard scatter process rather than simulate all possible *pp* collision scenarios. For a particular hard process, the incoming parton distributions are described by **P**arton **D**istribution **F**unctions (PDFs)[2] [66], and the probability distribution of the outgoing partons can be calculated by means of *perturbation theory* (cf. Section 2.3).

[1] *phenomenological fragmentation model*: due to the self-interacting property of gluons (cf. Section 2.2), colour field lines are compressed into tube-like regions ("strings") at large charge separations
[2] The notion of protons being made up of three quarks (uud) is an oversimplification that goes unnoticed

[2] parton showers
Scattered colour charges emit gluons, similar to how electric charges emit photons in QED, cf. Section 3.2.2 ("bremsstrahlung"). Once again, the difference is that gluons themselves are coloured (cf. Section 2.2) and can thus single-handedly trigger further gluon emissions. Analogous to the QED case, the QCD result is an extended cascade of partons (mostly gluons) with gradually decreasing energies.

[3] hadronisation
At some point in the partonic showering process, the momentum scale becomes so low that *perturbation theory* breaks down (cf. Section 2.3). At this stage, it is necessary to transition to *non-perturbative hadronisation* models that take into account the fact that partons are confined into bound hadronic states at these scales.

[4] underlying event
In the course of the hard process, coloured partons are scattered out of the protons, thus leaving the initially uncoloured protons in a coloured state. As a result, secondary interactions between the proton remnants occur and produce (predominantly) soft hadrons that contaminate the event. The entirety of secondary interactions form the so-called *underlying event*.

[5] unstable particle decays
There is no reason to assume that only stable hadrons are produced in stages **[3]** and [4]. Those that are unstable emerge as heavy resonances that decay further until only stable particles remain. Such incidents are taken into account in the final step of the event generation.

In the context of dijet searches with ATLAS, interesting events result from hard (i.e. involving high momentum transfers) $2 \to 2$ and $2 \to 3$ QCD processes such as those presented in Figure 2.4. In `PYTHIA`, hard processes for QCD jet production are selected by activating the common switch for the group of all hard QCD processes, i.e. `HardQCD:all = on`. *Three-jet topologies*, i.e. hard QCD processes with three partons in the final state (cf. Figure 2.4 (bottom)), are generated by showers of two-parton processes via `HardQCD:3parton = on` [67]. Note that a $2 \to 2$ hard scatter that is accompanied by either ISR or FSR can describe the same $2 \to 3$ process as a $2 \to 3$ ME. Consequently, `HardQCD:all` must be switched off if `HardQCD:3parton` processes are turned on to avoid double counting [55].

In either case, it is necessary to specify a sensible minimum jet p_T threshold. This is because the two aforementioned process groups use perturbative QCD cross sections

in the regime of low momentum transfers. In actual fact, a proton consists of so-called *valence quarks* - the quarks that determine its quantum numbers - which are embedded in a sea of virtual quark-antiquark pairs, cf. Section 2.2. PDFs are momentum distribution functions of the partons within the proton. They represent probability densities $f_i(x, Q^2)$ to find a parton of flavour i carrying a momentum fraction x of the proton momentum at a squared energy scale Q^2.

without any regularisation modifications [67], meaning that jet cross sections become unreasonably large if no minimum p_T threshold is specified or if the specified threshold is too low. Based on the p_T threshold for the leading (i.e. highest p_T) jet implemented in the ATLAS dijet angular analysis [68], namely $p_T > 440$ GeV, a phase space cut of $p_T > 380$ GeV is placed on the leading jet transverse momentum for the studies presented in this thesis to allow for comparisons and sanity checks with existing ATLAS results. The advantage of specifying a phase space cut for the jet p_T in the MC event generation that is slightly below the value used in the ATLAS analysis is that more events will pass the selection criteria (see Table 5.1), which in turn translates into a higher statistical significance and a reduced statistical error. Nonetheless, since the difference is small and the $p_T > 440$ GeV is rather conservative with respect to the trigger plateau (cf. Chapter 4), the results included in this thesis do not differ from the ones obtained in ATLAS analyses [48, 68] in a physically meaningful way.

In `PYTHIA`, the minimum invariant p_T can be specified as follows:[3]

$2 \to 2$ processes:
In a $2 \to 2$ (cf. Figure 2.4 (top)) process, symbolically $1 + 2 \to 3 + 4$, the minimum p_T threshold is set via the phase space parameter `PhaseSpace:pTHatMin`. Due to momentum conservation, the transverse momenta of the outgoing particles will balance before the occurrence of PSs, i.e. $p_{T_3} = p_{T_4}$. The parameter `PhaseSpace:pTHatMin` thus allows to specify a lower p_T boundary for both outgoing partons.

$2 \to 3$ processes:
In a $2 \to 3$ (cf. Figure 2.4 (bottom)) process, symbolically $1 + 2 \to 3 + 4 + 5$, the event is characterised by three separate p_T scales since there is no longer a complete balance between any pair of partons. For the purpose of phase space generation and cuts, these are arranged in descending order such that $p_{T_3} > p_{T_4} > p_{T_5}$. A minimum p_T threshold can be specified for the highest and lowest p_T parton using `PhaseSpace:pTHat3Min` and `PhaseSpace:pTHat5Min`, respectively. In doing so, the phase space available to p_{T_4} is restricted implicitly as the vector sum must satisfy $\boldsymbol{p_{T_3}} + \boldsymbol{p_{T_4}} + \boldsymbol{p_{T_5}} = 0$. In order to obtain a true *three-jet topology*, one has to ensure that all three outgoing partons carry significant energies. In particular, this implies that the phase space cut on `PhaseSpace:pTHat5Min` must not be too low with respect to `PhaseSpace:pTHat3Min`, or else the jet produced by the lowest p_T parton will have little to no impact on the event topology. Over the course of this study, the values `PhaseSpace:pTHat3Min = 380` and `PhaseSpace:pTHat5Min = 114` ($= 0.3 \cdot$`PhaseSpace:pTHat3Min`) were found to yield reasonable results. Hard $2 \to 2$ and $2 \to 3$ QCD processes will hereafter be referred to as *dijet* and *trijet topologies*, respectively. While both topologies are equally useful for modelling the SM background, the *trijet topology* is interesting in its own right as it has previously not been studied in depth with the `PYTHIA` event generator.

[3] Note that in `PYTHIA`, numerical values relating to energies and momenta are generally specified in units of GeV.

5.2 Dijet Observables

Physical objects like jets can be represented mathematically by *energy-momentum four-vectors* of the form [2]

$$p = p^\mu = \left(p^0, p^1, p^2, p^3\right) = (E, p_x, p_y, p_z) = (E, \boldsymbol{p}) \ . \tag{5.1}$$

By definition, the inner product of two *four-vectors*

$$p^2 = p \cdot p = p^\mu p_\mu = \eta_{\mu\nu} p^\mu p^\nu = E^2 - \boldsymbol{p}^2 = m^2 \ , \tag{5.2}$$

where $\eta_{\mu\nu} = \mathrm{diag}(1, -1, -1, -1)$ denotes the *Minkowski metric*[4] [69], is *Lorentz invariant*, i.e. the same in all reference frames with a uniform relative velocity [2]. This has profound implications for physics: From Equation (5.2), it is immediately clear that the particle mass m is an invariant quantity, which implies that the mass of a hypothetical new resonance can be deduced directly from the mass of its decay products, such as jets, for instance. This is precisely why searches for BSM phenomena examine the invariant mass distribution, cf. Section 4.1: If an excess of events were observed at a certain *dijet invariant mass* [50]

$$m_{jj} = E_{jj} - p_{jj} \ , \tag{5.3}$$

this would be a strong indication for the existence of a new particle that is not contained within the SM.

While an important observable, the invariant mass is certainly not the only way to look for new physics. BSM phenomena may also manifest themselves as deviations in the angular distribution of their decay products. In order to study angular distributions, it is necessary to introduce a few more variables.

Due to the composite nature of protons, the CM frame of particle collisions in the LHC rarely coincides with the detector rest frame. For this reason, it is useful to define the *rapidity* [70]

$$y := \frac{1}{2} \ln \left(\frac{E + p_z}{E - p_z} \right) \ , \tag{5.4}$$

where E denotes the particle energy and p_z the particle momentum along the z-axis ($\equiv$ beam axis, cf. Section 3.2.1). A nice property of this definition is that, analogous to the mass in Equation (5.2), *rapidity differences*

$$\Delta y_{ij} := |y_i - y_j| \tag{5.5}$$

between two particles i, j are conserved (i.e. invariant) under *Lorentz transformations* (informally often referred to as "Lorentz boosts") along the beam direction [70]. One can

[4] Note that $\eta_{\mu\nu} = \mathrm{diag}(-1, 1, 1, 1)$ is an equally appropriate choice.

show that the longitudinal *rapidity boost* y_B of a collision with respect to the detector frame can be expressed as the arithmetic mean of the rapidities y_3, y_4, of the outgoing partons, i.e. [50]

$$y_B = y - y_{CM} = \frac{|y_3 + y_4|}{2} \,, \tag{5.6}$$

where y_{CM} and y denote the rapidities measured in the CM and detector frame, respectively. Similarly, the quantity

$$y^\star = \frac{\Delta y_{34}}{2} = \frac{|y_3 - y_4|}{2} \quad , \quad \cos\hat{\theta} = \tanh y^\star \tag{5.7}$$

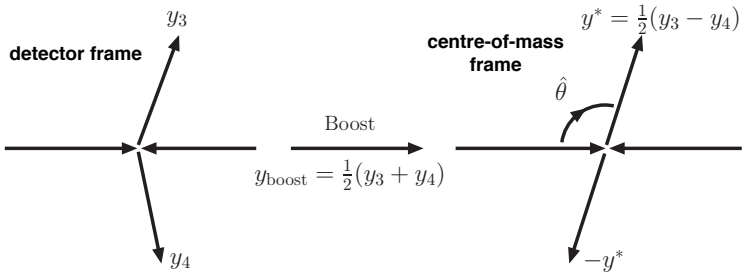

Figure 5.2: Schematic illustration of the rapidity boost y_B from the detector frame into the CM frame [71].

corresponds to the (equal in magnitude, but oppositely directed) parton rapidities in the CM frame, see Figure 5.2. In the context of dijet events, y_B and $y^\star$ can be interpreted as a measure of the angle that is comprised by the two jet cones. This is illustrated in Figure 5.3.

Using the above definition of $y^\star$, it is possible to define a *rapidity difference measure* [50]

$$\chi := e^{2|y^\star|} = e^{|y_3 - y_4|} = \frac{1 + |\cos\hat{\theta}|}{1 - |\cos\hat{\theta}|} \propto \frac{1}{1 - |\cos\hat{\theta}|} \,, \tag{5.8}$$

where θ denotes the CM *scattering angle*, cf. Figure 5.2. This parameter is extremely useful in the study of angular distributions, as will become evident in Section 5.5.

The rapidity is often paired with the azimuthal angle ϕ (cf. Section 3.2.1) to define the *angular separation*

$$\Delta R := \sqrt{(\Delta y)^2 + (\Delta\phi)^2} \tag{5.9}$$

of two objects, e.g. partons and/or jets. Note that, by definition, ΔR is also invariant with respect to *Lorentz boosts* along the beam direction. It will become the main interest in Section 5.5.3.2.

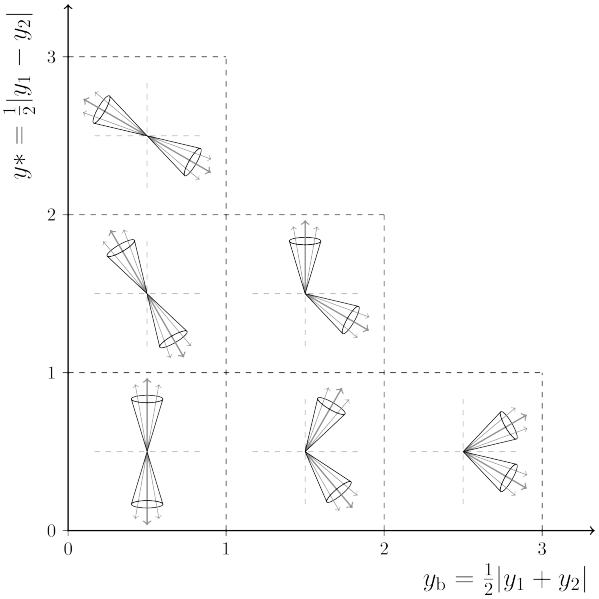

Figure 5.3: Visualisation of the spatial alignment of dijet event topologies in the y^*-y_B-plane [72].

Unfortunately, rapidities are extremely difficult to measure for highly relativistic particles since measurements of a particle momentum's z component ($\equiv$ beam direction, cf. Section 3.2.1) are obstructed by the LHC beam pipe. However, note that in the relativistic limit, where particle rest masses become negligible, the rapidity approaches[5]

$$y = \frac{1}{2}\ln\left(\frac{E+p_z}{E-p_z}\right) = \frac{1}{2}\ln\left(\frac{\sqrt{p^2c^2+m^2c^4}+p_zc}{\sqrt{p^2c^2+m^2c^4}-p_zc}\right) \tag{5.10}$$

$$\overset{pc\gg mc^2}{\simeq} -\ln\left[\tan\left(\frac{\theta}{2}\right)\right] =: \eta \qquad \text{using} \quad \frac{p_z}{p} = \cos\theta \quad (\rightarrow \text{see Section 3.2.1}) \tag{5.11}$$

This motivates the definition of *pseudorapidity* as in Section 3.2.1, cf. Equation (3.1) and Figure 3.4.

5.3 Kinematic Selection and Phase Space Cuts

To allow for comparisons to existing data, results presented in this thesis are generated using the same kinematic selection in the MC event generation as is used in the ATLAS dijet angular analysis [68]. To achieve this, the `C++` code written for the work in this thesis makes use of the `SlowJet` class [67] for jet finding according to the anti-k_t algorithm (cf. Section 4.2.2), implemented in `PYTHIA`. An explanation for the individual choices made is provided in [48, 50, 68, 71]. In a simplified scheme, the line of thought is as follows:

[5] See [70] for a detailed derivation. To avoid ambiguity, the convention of using natural units is rescinded for this equation only.

1. Since BSM phenomena are predicted to cause alterations in the partonic cross section measured by ATLAS, it is desirable to maximise the sensitivity of this measurement.
2. For this purpose, selection cuts in (pseudo)rapidity (η)y are applied, following the procedure outlined in [71].
3. In order to avoid bias from single jet triggers ($\rightarrow$ *trigger efficiency*, *turn-on curve*), a cut is placed on the transverse momentum p_T of the leading jet [48].
4. The lowest possible invariant mass m_{inv} that can be measured without introducing a bias resulting from the p_T cut is predefined by the p_T threshold and the chosen χ range [71] (the lowest order expression is derived in Section 5.5.2, see Equation (5.20)).
5. When choosing the χ range, a compromise must be made between extensive statistics and search sensitivity.

The numerical values used by the ATLAS dijet angular analysis [68] are summarised in the form of their corresponding phase space parameters in `PYTHIA` in Table 5.1. Unless specified otherwise, all histograms presented in Sections 5.4 and 5.5 were produced using these values. Note that all histograms presented in Section 5.4 and Section 5.5.1 were generated using the same number of events for each distribution. This is not necessarily the case in Sections 5.5.2 and 5.5.3, where histograms have been normalised to unit area. This thesis is only concerned with the expected SM background, i.e. no BSM signals have been included in this study.

Summary of kinematic selection and phase space cuts			
		Dijet topology	**Trijet topology**
Kinematic Selection Cuts	leading	`slowjet.p(0)` > 440 GeV	
	subleading	`slowjet.p(1)` > 50 GeV	
	all	`pTmin` ≥ 50 GeV	
Kinematic Phase Space Cuts		`PhaseSpace:mHatMin = 2400`	
	leading	`PhaseSpace:pTHatMin = 380`	`PhaseSpace:pTHat3Min = 380`
	subsubleading	-	`PhaseSpace:pTHat5Min = 114`
Angular Selection Cuts		$\lvert y^\star \rvert < 1.7$	
		$\lvert y_B \rvert < 1.1$	
		-	`PhaseSpace:RsepMin = 1`

Table 5.1: Summary of kinematic selection and phase space cuts.

5.4 Kinematic Variables

5.4.1 Transverse Momentum

Jet p_T distributions for the *leading* (highest p_T), *subleading* (second highest p_T) and *subsubleading* (third highest p_T) *jet* are presented in Figure 5.4 for the dijet (black) and trijet (light blue) event topologies introduced in Section 5.1. It is worth noting that

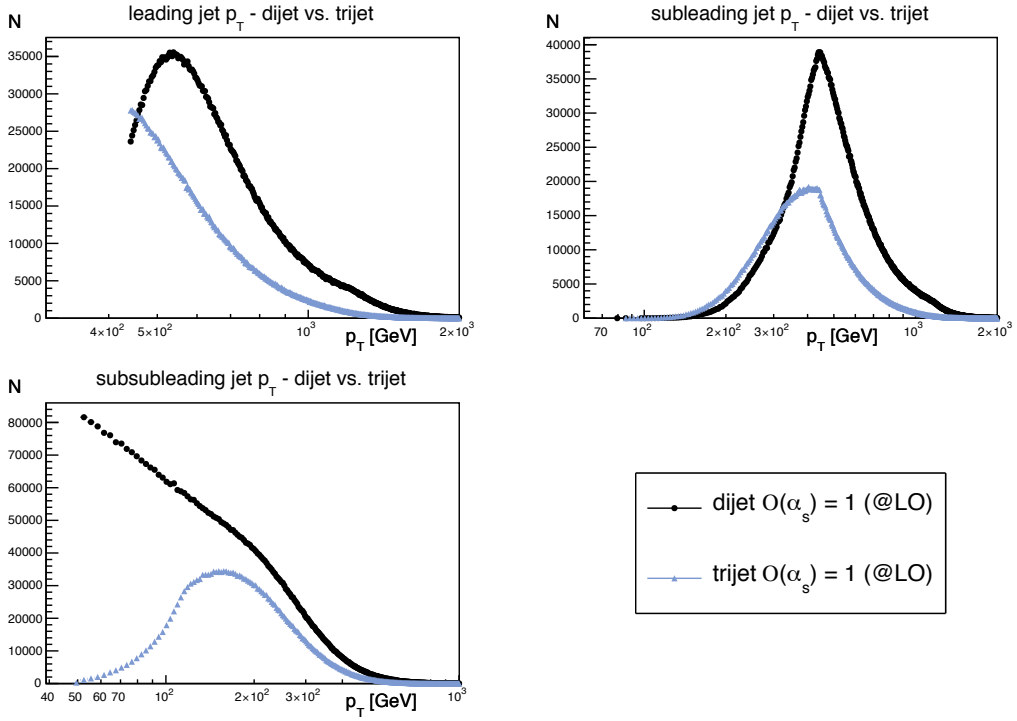

Figure 5.4: Jet p_T distributions of the three highest p_T jets in dijet vs. trijet event topologies.

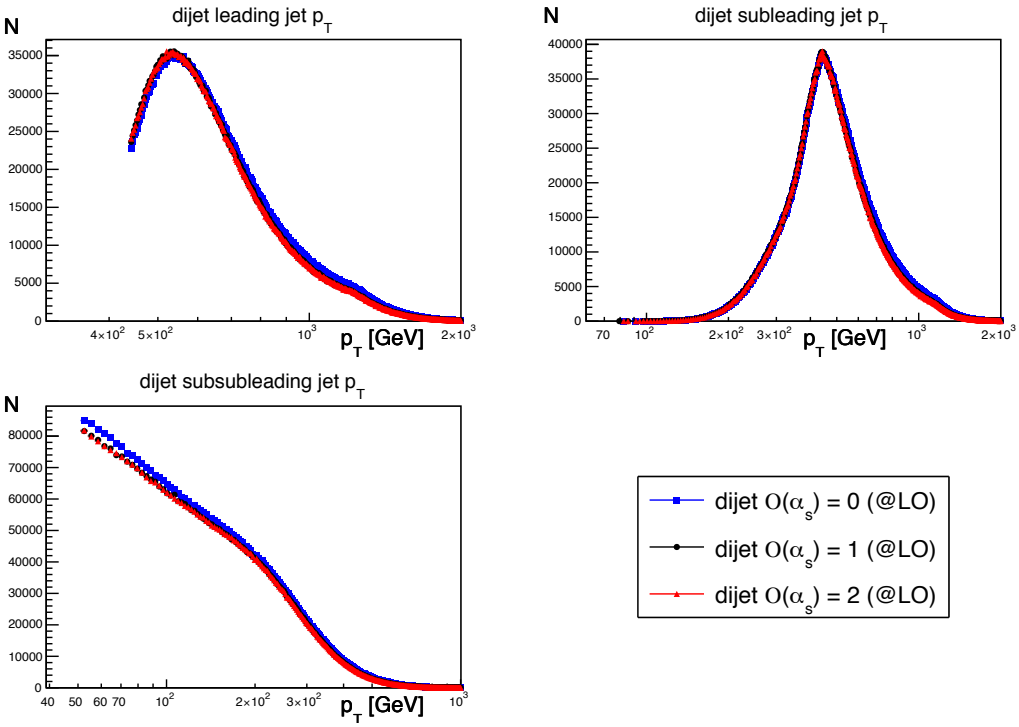

Figure 5.5: Jet p_T distributions of the three highest p_T jets in the dijet topology for three different running orders $\mathcal{O}(\alpha_s) \in \{0, 1, 2\}$ of the strong coupling constant α_s.

- if no additional constraints are imposed, jet p_T distributions are steeply falling, i.e. low p_T ("soft") jets are more common than high p_T ("hard") jets, cf. discussion in Section 4.1.

- one can recover many features that appear due to the kinematic selection outlined in Section 5.3. In particular:
  - in both event topologies, the minimum p_T threshold specified for the leading (subleading) jet is $p_T > 440$ GeV (> 50 GeV).
  - only jets that satisfy $p_T \geq 50$ GeV are stored by the `Slowjet` algorithm.
  - the fraction of events that pass the event selection criteria is higher in the dijet as compared to the trijet case.
  - the minimum p_T threshold specified for the subsubleading jet in the trijet topology is $p_T \geq 114$ GeV. This gives rise to a peak at $p_T \approx 108$ GeV. In contrast, the subsubleading jet distribution of the dijet event topology peaks right at the threshold of $p_T \geq 50$ GeV implemented in the `Slowjet` jet finder, as one would expect from a steeply falling distribution that is not subjected to additional restrictions (such as the minimum p_T threshold in the trijet topology).
  - higher p_T scales are reached in the dijet topology, see histograms for leading and subleading jet distributions. This is can be ascribed to
    * the impact of the the kinematic selection discussed above, i.e. because the subsubleading jet is harder in the trijet event topology, and thus the phase space available to the remaining two highest p_T jets is reduced in comparison with the dijet topology.
    * the fact that, because of the way momentum is balanced in the two topologies (see discussion in Section 5.1), leading and subleading jets are more likely to be emitted *back-to-back* (i.e. comprising large angles) in the dijet topology, as can be seen in Section 5.5.1, for instance.

With `PYTHIA`, it is also possible to study p_T distributions at different running orders $\mathcal{O}(\alpha_s)$ of the strong running coupling constant α_s, cf. Equation (2.6). The parameter `SigmaProcess:alphaSorder` (hereafter abbreviated as $\mathcal{O}(\alpha_s)$) is designated for this purpose, where $\mathcal{O}(\alpha_s) = 0$ corresponds to a constant value of α_s (i.e. no energy scale dependence), $\mathcal{O}(\alpha_s) = 1$ to the first order expression provided in Equation (2.6), and $\mathcal{O}(\alpha_s) = 2$ to a calculation of α_s up to second order. Results are presented for the dijet topology in Figure 5.5. As one can see, there is a general trend to obtain slightly more events at lower running orders. Note that the $\mathcal{O}(\alpha_s) = 1$ (black) line, which is mostly concealed between $\mathcal{O}(\alpha_s) = 0$ (blue) and $\mathcal{O}(\alpha_s) = 2$ (red), corresponds to the dijet distributions shown in Figure 5.4.

In principle, it is possible to study this behaviour for other variables such as invariant mass m_{inv}, rapidity y, etc. as well. However, no new information is contained within

the resulting distributions, since they can - in theory - be reconstructed from the jet p_T distributions presented in Figure 5.5. Analogously, the same is true for the trijet topology. For the sake of illustration, the dijet topology results are included in this thesis, but without further elaborations, see Appendix A.

5.4.2 Invariant Mass

The importance of the invariant mass for BSM searches has been highlighted throughout this thesis. In the dijet topology, it is simply reconstructed from the momenta of the two highest p_T jets according to Equation (5.3). In the `C++` code that uses the `PYTHIA` classes written for the work in this thesis, the invariant mass can be reconstructed by passing the four-vectors (cf. Equation (5.1)) of leading and subleading jet to the member function `double m(const Particle& pp1,const Particle& pp2)`, i.e.

```
1   double invM;
2   Vec4 p0,p1;
3   p0 = slowjet.p(0);    // leading jet
4   p1 = slowjet.p(1);    // subleading jet
5   invM = m(p0,p1);
```

In the trijet topology, the invariant mass can either be defined in the same way, or, one could include the subsubleading jet in the definition of the invariant mass, i.e.

```
1   double invM;
2   Vec4 p0,p1;
3   p0 = slowjet.p(0);    // leading jet
4   p1 = slowjet.p(1)+slowjet.p(2);  // subleading + subsubleading jet
5   invM = m(p0,p1);
```

Both options available for the trijet topology, labelled trijet$_{\mathrm{m2}}$ (beige) and trijet$_{\mathrm{m3}}$ (light blue) for the two-jet and three-jet definition, respectively, are displayed together with the dijet topology in Figure 5.6. If the trijet invariant mass is defined in the same way as in the dijet case, the invariant mass distribution deviates from the expected shape since part of the invariant mass, namely the fraction that is carried by the subsubleading jet, is missing from the event. If, on the other hand, the subusbleading jet is included in the definition of the trijet invariant mass, the two distributions (dijet vs. trijet) exhibit the same form. Also, note that both distributions peak at $m_{\mathrm{inv}} = 2400$ GeV in accordance with the phase space cut specified via `PhaseSpace:mHatMin`, see Table 5.1. Due to the missing mass in the trijet$_{\mathrm{m2}}$ definition, this peak is shifted towards lower invariant masses in the trijet$_{\mathrm{m2}}$ distribution. Again, fewer events are contained in the trijet distributions as the *selection criteria* are more demanding, cf. Section 5.3.

To illustrate the impact of the phase space cut placed on the invariant mass, distributions that were generated using the default value `PhaseSpace:mHatMin = 4` [67] are presented separately in Figures 5.7 to 5.9 for the three distinct cases.

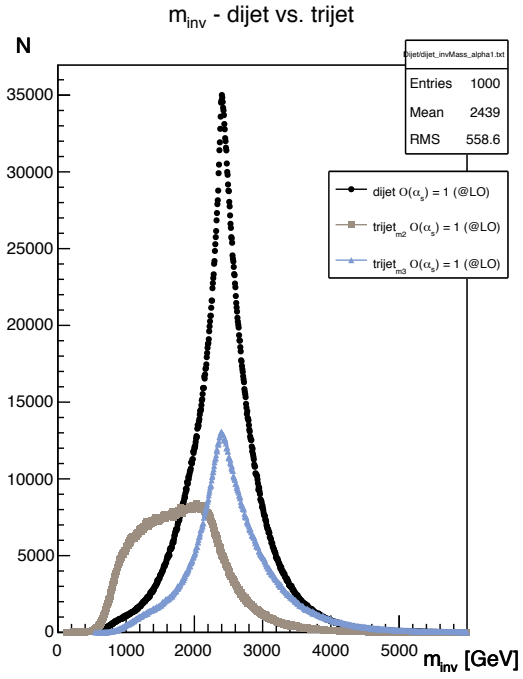

Figure 5.6: Invariant mass distributions for the dijet and trijet topology. Two definitions, labelled `trijet`$_{m2}$ and `trijet`$_{m3}$, are possible for the latter.

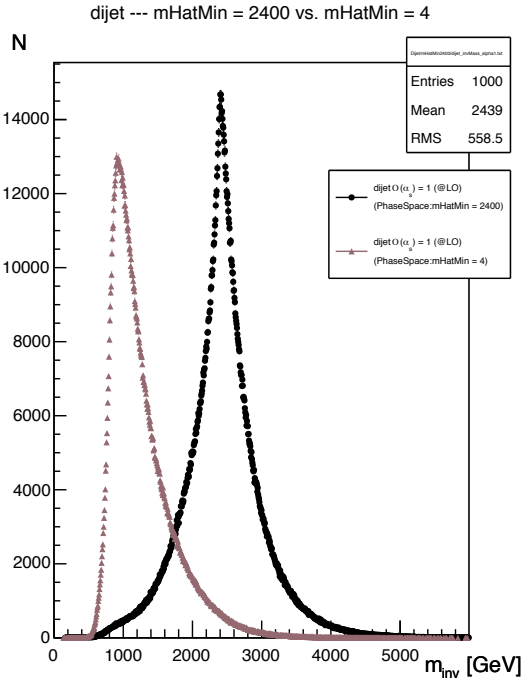

Figure 5.7: Impact of the phase space cut placed on the invariant mass in the dijet topology.

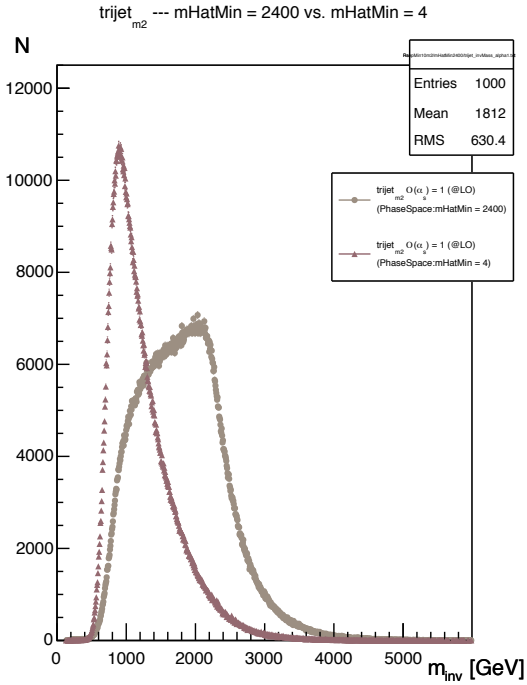

Figure 5.8: Impact of the phase space cut placed on the invariant mass in the `trijet`$_{m2}$ definition of the trijet topology.

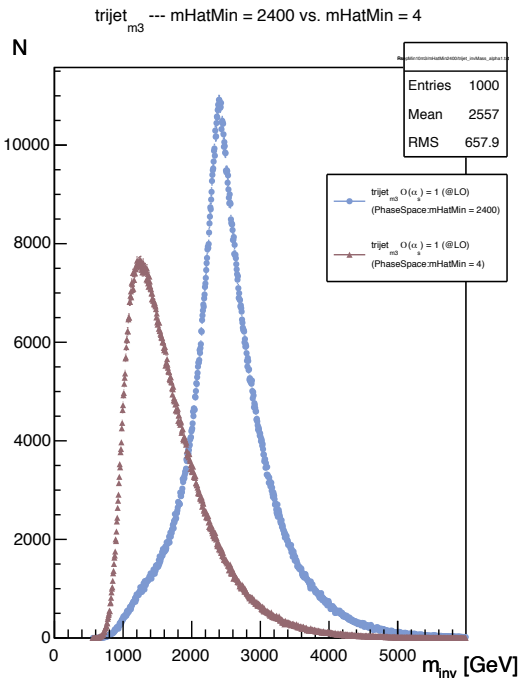

Figure 5.9: Impact of the phase space cut placed on the invariant mass in the `trijet`$_{m3}$ definition of the trijet topology.

5.5 Angular Distributions

5.5.1 Rapidity Variables

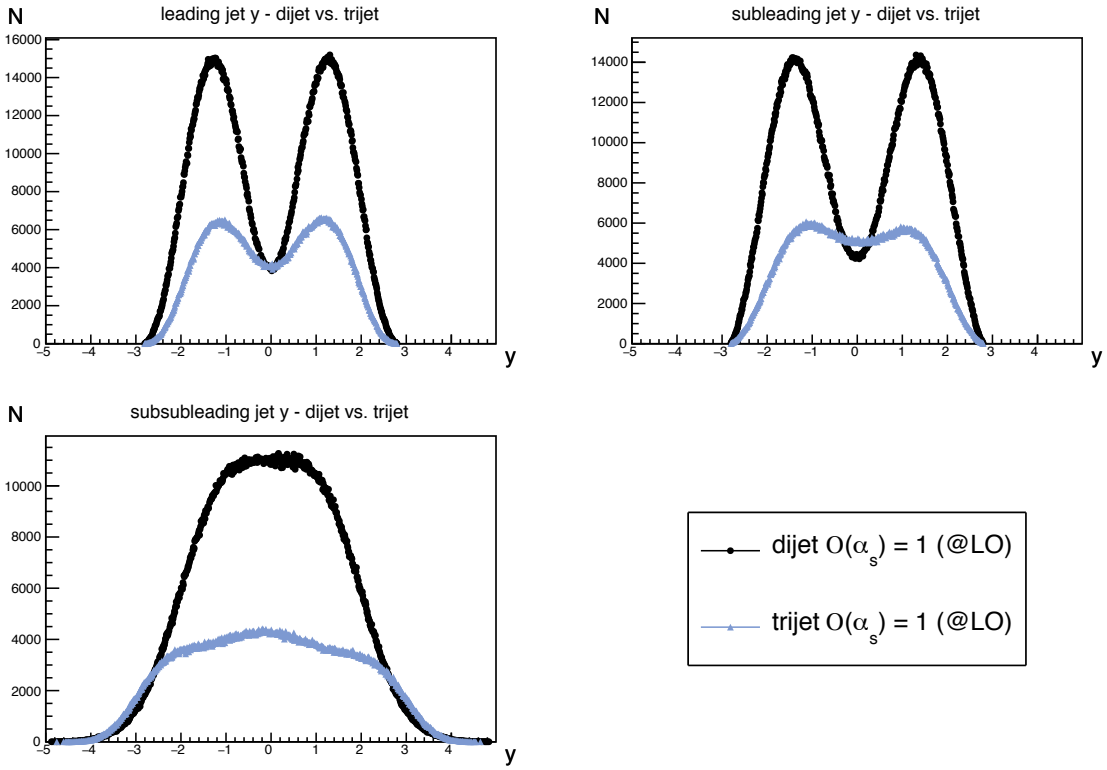

Figure 5.10: Rapidity distributions of the leading, subleading, and subsubleading jet for dijet (black) and trijet (light blue) event topologies.

Before studying more complex variables such as χ, it can be helpful to first familiarise oneself with the rapidity variables y, y_B and $y^\star$. The leading, subleading, and subsubleading jet rapidity distributions are shown for dijet and trijet event topologies in Figure 5.10. The most striking features are:

- in the dijet topology, leading and subleading jet rapidity distributions share the same features and cannot be distinguished: they comprise two local maxima at $y \approx \pm 1.5$ that exhibit axial symmetry with respect to the local minimum at $y = 0$. The latter results from the kinematic selection (cf. Section 5.3), more specifically the phase space cut that is placed on the invariant mass, cf. Section 5.4.2. This can be inferred rather intuitively from Equation (5.20): The LO effect of implementing a threshold for the minimum invariant mass is to bias the rapidity distributions towards greater angular separations between the jet pairs.
- in the trijet topology, leading and subleading jet rapidity distributions are not

symmetric with respect to $y = 0$; this is due to the fact that in the trijet topology, there exists no longer a complete balance of parton momenta, cf. discussion in Section 5.1.

- the "dip" at $y = 0$, i.e. the visible impact of the phase space cut on the invariant mass, is less pronounced in the trijet topology; this can be attributed to the fact that the two leading jets are generally softer in the trijet topology as compared to the dijet topology, cf. Figure 5.4.
- similarly, the fact that no pronounced "dip" is observable in either of the subsubleading jet rapidity distributions can most likely be traced back to the lower p_T scales; however, the fact that the distributions do not exhibit a narrow peak, as one would naively expect, could be an indication that they are not completely unaffected by the phase space cut on the invariant mass either.

For completeness, the distributions of the complementary variables y_B and $y^\star$ are presented in Figure 5.11. They can be inferred from the y distributions shown in Figure 5.10 according to Equations (5.6) and (5.7).

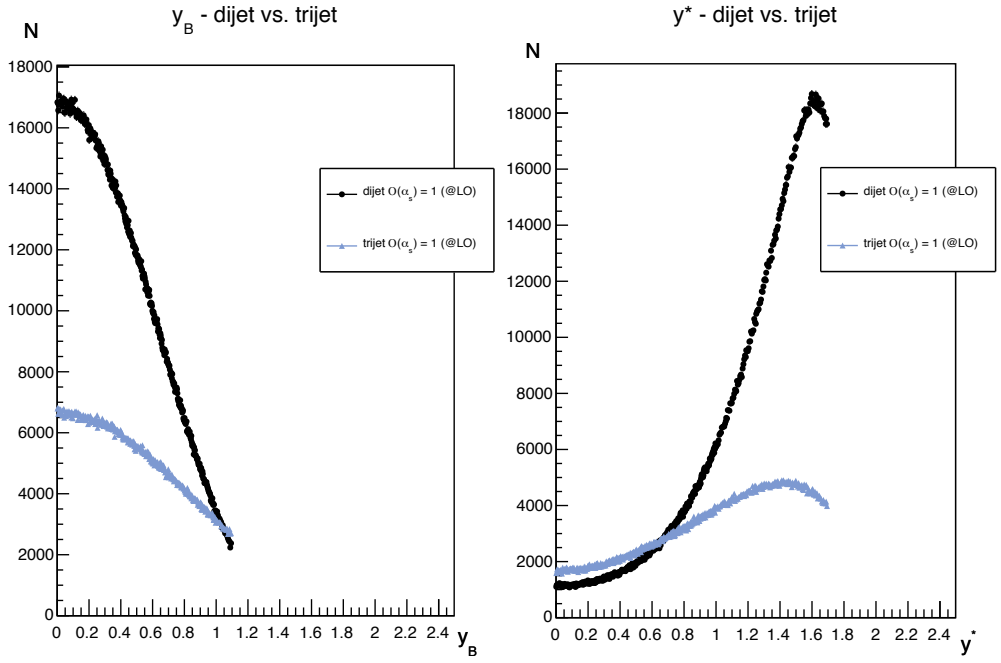

Figure 5.11: Comparison of y_B (left) and $y^\star$ (right) distributions in the dijet vs. trijet topology.

5.5.2 Dijet Angular Distribution

To describe the kinematics of a $1+2 \to 3+4$ scattering process and derive cross sections, it is convenient to introduce the *Mandelstam variables* [2, 3]:

$$\hat{s} := (p_1 + p_2)^2 \ , \tag{5.12}$$

$$\hat{t} := (p_1 - p_3)^2 = -\frac{\hat{s}}{2}\left(1 - \cos\hat{\theta}\right) \ , \tag{5.13}$$

$$\hat{u} := (p_2 - p_3)^2 = -\frac{\hat{s}}{2}\left(1 + \cos\hat{\theta}\right) \ , \tag{5.14}$$

where $\hat{\theta}$ denotes the CM scattering angle (see Figure 5.2) and $\hat{s}$ the squared CM energy in the parton-parton frame. The *differential partonic cross section* is given by [50, 71]

$$\frac{d\hat{\sigma}}{d\hat{t}} = \frac{1}{2\hat{s}^2}\frac{1}{8\pi}\overline{\sum}|\mathcal{M}|^2\delta^4\left(p_1 + p_2 - p_3 - p_4\right) \propto \frac{1}{\hat{s}^2}\overline{\sum}|\mathcal{M}|^2 \ , \tag{5.15}$$

where the notation $\overline{\sum}|\mathcal{M}|^2$ for the squared matrix elements implies the averaged sum of all initial and final state colours and spins. For the dominant process $qq' \to qq'$ at high energies, one can derive that [50]

$$\overline{\sum}|\mathcal{M}|^2 \propto \alpha_s^2\frac{\hat{s}^2 + \hat{u}^2}{\hat{t}^2} \overset{\substack{|\hat{t}|\leq\hat{s}\\ |\hat{u}|\leq\hat{s}}}{\approx} \alpha_s^2\frac{\hat{s}^2}{\hat{t}^2} \ . \tag{5.16}$$

Inserting this expression into Equation (5.15) yields the following approximation:

$$\frac{d\hat{\sigma}}{d\hat{t}} \propto \frac{\alpha_s^2}{\hat{t}^2} \ . \tag{5.17}$$

Using Equations (5.8) and (5.13) and keeping $\hat{s} = \text{const.}$ (or, experimentally, $m_{\text{inv}} = \text{const.}$), this expression can be rewritten as a function of the rapidity difference measure χ, i.e.

$$\frac{d\hat{\sigma}}{d\chi} \propto \frac{\alpha_s^2}{\hat{s}} \ . \tag{5.18}$$

Therefore, the differential cross section of a $2 \to 2$ scattering process ($\hat{t}$-channel exchange) is approximately constant at lowest order.

On the other hand, many hypothetical new resonances are typically predicted to decay *isotropically*, that is independently of $\hat{\theta}$ [71]. In this case, one finds that

$$\frac{d\hat{\sigma}}{d\left(\cos\hat{\theta}\right)} \propto \text{const.} \quad \Rightarrow \quad \frac{d\hat{\sigma}}{d\chi} \propto \frac{1}{\left(1 + \chi\right)^2} \ , \tag{5.19}$$

i.e. the cross section will peak at low values of χ. This is in sharp contrast with the previously derived QCD scattering cross section (cf. Equation (5.18)), as is illustrated in Figure 5.12. Due to the substantial differences in the shape of the distributions for a fixed $\hat{s}$, it is suitable to bin the cross section in bins of invariant mass. At LO, one finds that [50, 71]

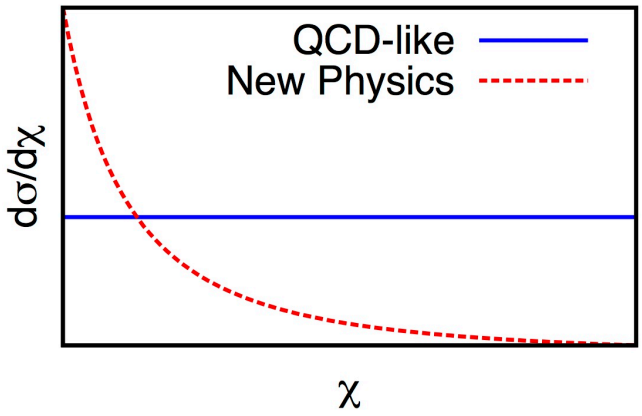

Figure 5.12: Schematic illustration of angular distribution cross sections expected from QCD (continuous blue line) and BSM (dashed red line) processes [71].

$$\sqrt{\hat{s}} = m_{\text{inv}} = 2p_T \cosh\left(|y^\star|\right) = p_T \left(e^{|y^\star|} + e^{-|y^\star|}\right) = p_T \left(\sqrt{\chi} + \frac{1}{\sqrt{\chi}}\right) , \tag{5.20}$$

i.e. in the lowest order approximation, high p_T jets are found at low χ for a given invariant mass. The mass intervals used in this thesis were chosen so as to coincide with [68]. Regarding the binning of χ, one should consider:

1. Interesting physics is expected to occur at low χ. Hence, the binning must allow for detailed shape comparisons in this regime.

2. Migrations across bin borders should be kept at a minimum in order to reduce the impact on a measurement.

A detailed study conducted in [71] concluded that bin edges b_i distributed in the range $\chi \in [1, 30]$ according to the exponential function

$$b_i = e^{0.3 \cdot i} \quad , \quad i \in \mathbb{N}_0 \tag{5.21}$$

$$\Rightarrow \quad b_i = \{1.000, 1.350, 1.822, 2.460, 3.320, 4.482, 6.050, 8.166, 11.023, 14.880, 20.086, 30.000\} \tag{5.22}$$

are ideal. Note that the angular selection cut $|y^\star| < 1.7$ corresponds to $\chi \approx 29.96$. The last bin edge is thus an exception to the above formula and has been visually extended to $\chi = 30.000$.

As the name implies, the rapidity difference measure χ can be reconstructed from the rapidities of the two leading jets, cf. Equation (5.8). One of the main objectives of this thesis was to study the behaviour of angular distributions of both dijet and trijet topologies using the MC generator `PYTHIA 8.219`. Due to the distinct differences between signal and background (see Figure 5.12), angular distributions are among the most

promising signatures in the search for new physics, and are thus well established as one of the main areas of particle physics research at Lund University, see [50, 68, 71].

For instance, one can examine the variation of angular distributions at different running orders $\mathcal{O}(\alpha_s)$ of the strong coupling constant α_s. The result for the dijet topology is shown in Figure 5.14[6]. At first glance, all three distributions are approximately flat (note that the y-axis range displayed in Figure 5.14 is very small!) over the whole χ range. This is the result one would expect from the lowest order approximation, cf. Equation (5.17). On closer examination, however, one can observe that all three distributions tend to rise in the low χ regime, particularly in the first two bins. While this behaviour is not predicted by the lowest order expression obtained in the simplified derivation provided above, it can be inferred from the χ-dependence of QCD subprocess MEs, see Figure 5.13 (note that a linear x-axis scale is used this figure!).

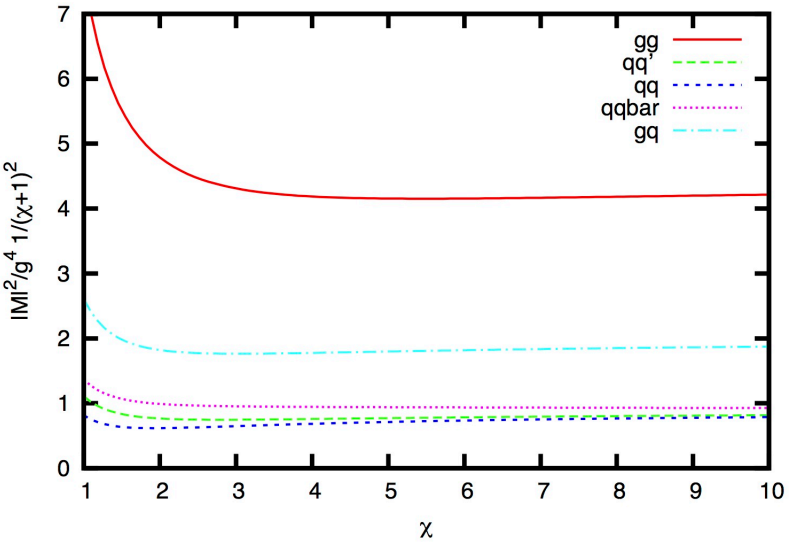

Figure 5.13: χ-dependence of QCD subprocess MEs for $\hat{s} = 1$ GeV [71].

While $\mathcal{O}(\alpha_s) = 2$ and $\mathcal{O}(\alpha_s) = 1$ are barely distinguishable, $\mathcal{O}(\alpha_s) = 0$ generally produces larger bin contents, which is in agreement with the effect seen in the distributions of other variables, for instance transverse momentum (Figure 5.5), invariant mass (Figure A.1) and rapidity (Figure A.2). Moreover, the difference between the lowest order $\mathcal{O}(\alpha_s) = 0$ and the higher orders $\mathcal{O}(\alpha_s) = 1$ and $\mathcal{O}(\alpha_s) = 2$ is more pronounced in the low χ regime. In fact, all three orders are approximately equal in the range $\chi \in [10, 20]$, and the higher orders are typically above the lowest order in the last bin, i.e. for $\chi \in [20, 30]$. Since events with high invariant masses and low χ values are less common, statistical errors are larger in the regime of low χ and for distributions of higher mass intervals. This generic feature is present in all *chi* distributions discussed in this thesis.

[6] Since $N \propto \hat{\sigma}$, distributions of the form $\frac{1}{N}\frac{dN}{d\chi}$ vs. χ have the same physical meaning as distributions of the form $\frac{d\hat{\sigma}}{d\chi}$ vs. χ, for instance in Figure 5.12.

In a BSM search with ATLAS data, one would usually normalise the SM prediction to have the same integral as the data. This has several advantages: Most importantly, searches for new phenomena rely heavily on the ability to identify deviations in the data from the predicted SM behaviour. It is thus desirable to minimise uncertainties in the modelling of the SM background as much as possible. In this thesis, all χ distributions have been normalised to unit area following the same procedure, that is via division by number of events and bin width. This is more convenient from a practical point of view as it allows compare different dataset even if they do not comprise the same number of events. In addition, it allows for cross-comparisons to [50, 68].

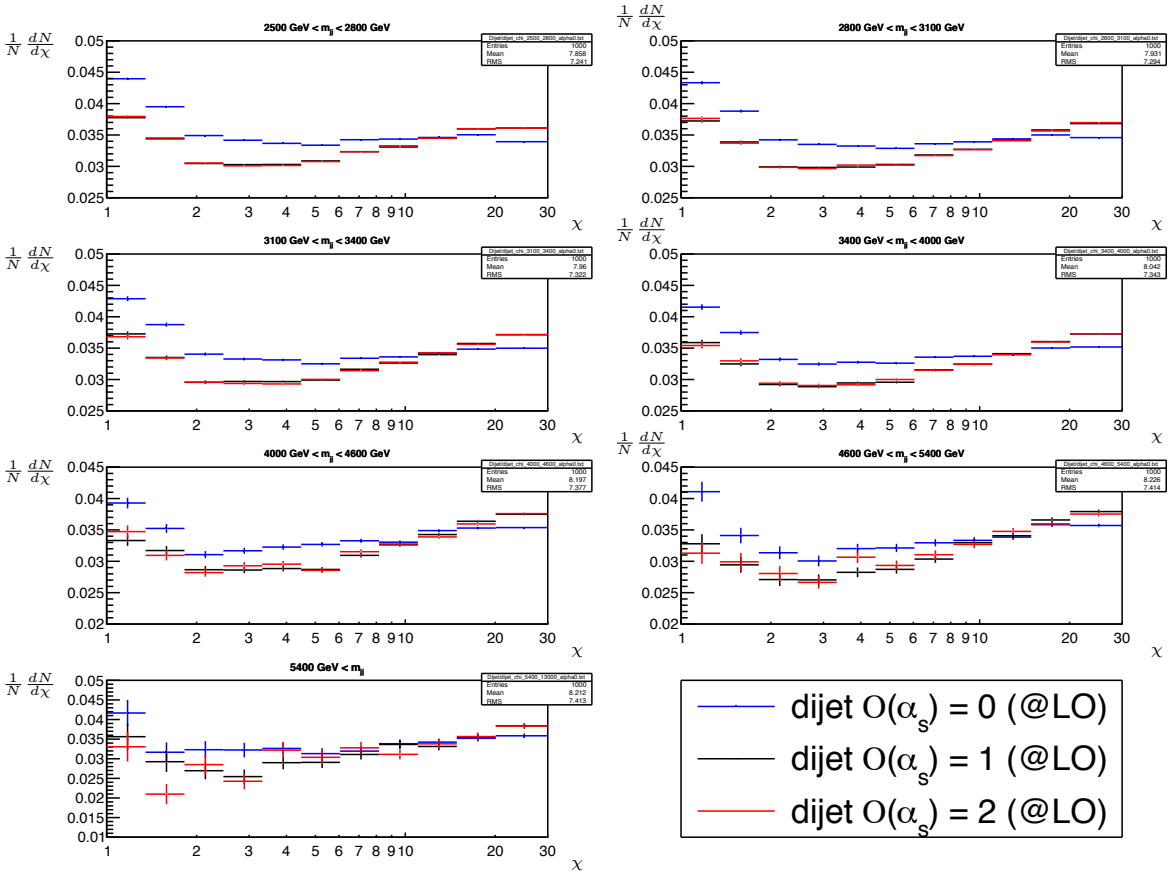

Figure 5.14: Normalised angular distributions for the dijet topology at different running orders $\mathcal{O}(\alpha_s)$ of the strong coupling constant α_s.

5.5.2.1 Application of NLO Corrections

By default, `PYTHIA` allows to make predictions for QCD processes up to LO only. Since it is a complete event generator (cf. Section 5.1), some of the missing contributions from higher order processes are partially compensated through the implementation of **P**arton **S**howers (PS). In a hard $2 \to 2$ scattering process, for instance, NLO contributions such

as an additional jet are already accounted for at LO via ISR (or FSR) off of one of the initial (final) state partons, cf. Figure 2.4. Nevertheless, this does not correspond to the same level of precision as a fully developed perturbative NLO calculation. However, it is possible to improve the PYTHIA prediction up to NLO accuracy via the bin-wise application of correction factors, abbrev. k-factors. These bin-by-bin correction factors are derived from **M**atrix **E**lement type MC generators (cf. Section 5.1), in this case NLOJET++ [73, 74], as the ratio between NLO and **L**eading **O**rder (LO) cross sections.

Of course, the fact that non-perturbative contributions are already included in the PYTHIA LO prediction has to be taken into account. One can identify the difference between the pure LO and partially corrected LO result by running a dedicated incomplete sample, i.e. using only stages **[1]** and [2] of the event generation chain (cf. Section 5.1) and deactivating all non-perturbative processes. The NLO corrected result can then be obtained as follows:

$$\mathcal{P}_{NLO} = \mathcal{P}_{\text{compl}} \cdot \frac{\mathcal{N}_{NLO}}{\mathcal{N}_{LO}} \frac{\mathcal{P}_{LO}}{\mathcal{P}_{PS}} \quad \text{with} \quad k_{\text{fac}} := \frac{\mathcal{N}_{NLO}}{\mathcal{N}_{LO}} \frac{\mathcal{P}_{LO}}{\mathcal{P}_{PS}} \quad , \tag{5.23}$$

where $\mathcal{P}$ and $\mathcal{N}$ denote PYTHIA and NLOJET++ generated MC samples. The subscripts indicate sample generation with **L**eading **O**rder **M**atrix **E**lements (LO), **N**ext-to-**L**eading **O**rder **M**atrix **E**lements (NLO), **L**eading **O**rder with **P**arton **S**howers only (PS) and a complete sample including all stages of the event generation chain, including non-perturbative effects (compl). One should be aware that this derivation rests on the assumption that the two LO matrix calculations $\mathcal{P}_{LO}$ and $\mathcal{N}_{LO}$ are equivalent. This can be achieved by choosing the same PDFs input and using the same numerical value for the strong coupling constant α_s.

The angular distribution of the $\mathcal{P}_{NLO}$ result, referred to from here on as *NLO corrected dijet topology*, is presented together with the LO dijet topology in Figure 5.15 at running order $\mathcal{O}(\alpha_s) = 1$. As can be seen, the NLO corrected results generally tend to have higher event yields across the whole χ range. However, note that it is not possible to intuitively predict the impact of these loop corrections, especially since they certainly depend on the physical parameters used by the jet finder algorithm, for instance the jet cone radius [75]. Analogous to Figure 5.14, both distributions show a small rise in the low χ regime, as one would expect according to Figure 5.13. The two distributions are very similar in shape, except for minor differences in the last three bins ($\chi > 10$), where the LO distributions seem to exhibit a slow rise, while the NLO corrected results tend to be a little more flat. Note that the trijet topology cannot be corrected in the same way since k-factors are currently not available for this process.

5.5.3 Trijet Angular Distribution

5.5.3.1 Weighted vs. Unweighted Angular Distributions

ME calculations (cf. Section 5.1) must be performed using the same value α_s for all vertices of a particular graph in order to guarantee a consistent addition of transition

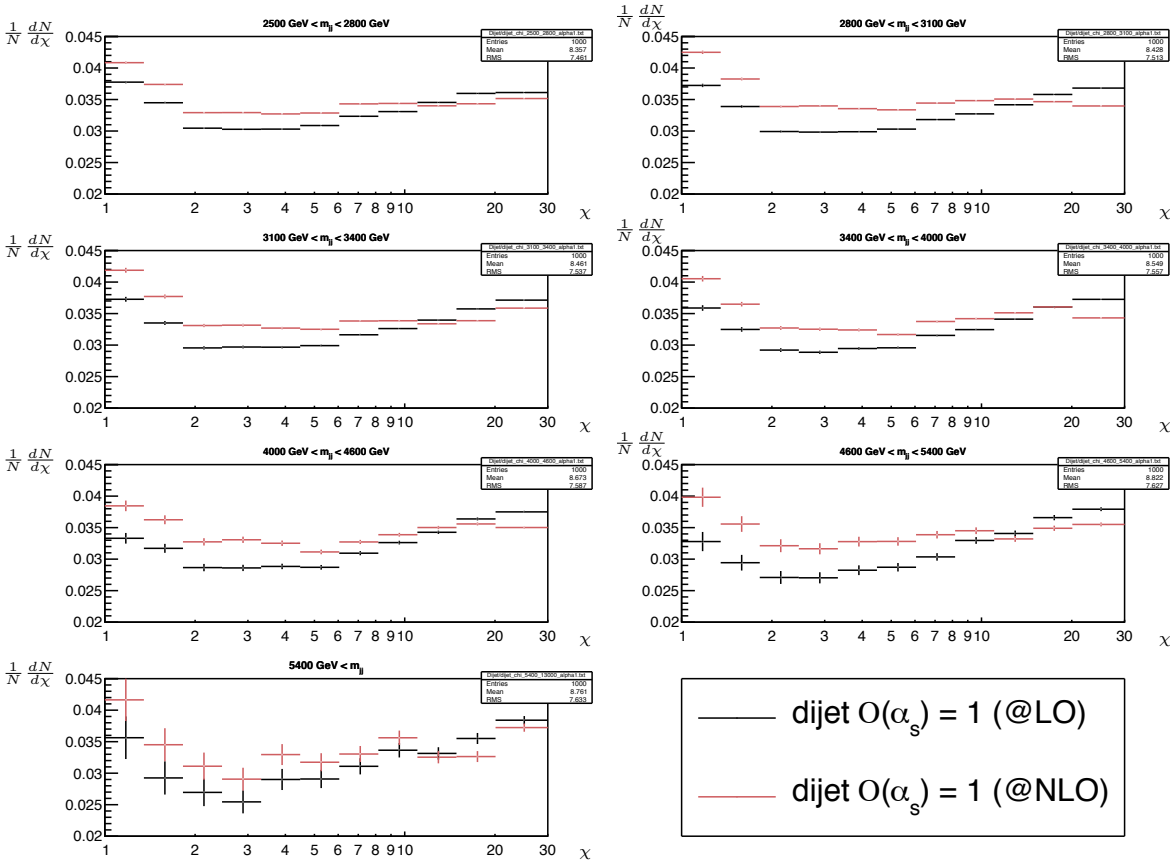

Figure 5.15: Normalised angular distributions for the dijet and NLO corrected dijet topology at $\mathcal{O}(\alpha_s) = 1$.

amplitudes. From Equation (2.6), it is clear that the α_s scale associated with soft emissions such as ISR and FSR should be much smaller than that of the hard process, i.e. for the two leading jets. In order to correct for this effect, one can introduce a *weight factor*

$$\kappa := \frac{\alpha_s(p_{T_5})}{\alpha_s(p_{T_3})} \overset{2.6}{=} \frac{\ln\left(p_{T_3}^2/\Lambda_{QCD}^2\right)}{\ln\left(p_{T_5}^2/\Lambda_{QCD}^2\right)} \quad \text{with} \quad p_{T_3} > p_{T_5} \;\;,\;\; \Lambda_{QCD} \simeq 0.2 \text{ GeV} \;, \tag{5.24}$$

where p_{T_3} and p_{T_5} denote the transverse momenta of the leading and subsubleading jet, respectively (cf. notation in Section 2.2). The result of this correction is presented together with the unweighted case in Figure 5.16. The dijet topology is included for comparison. The bottom panel displays the bin-by-bin ratio (labelled "$\mathcal{R}$") of weighted to unweighted trijet distributions.

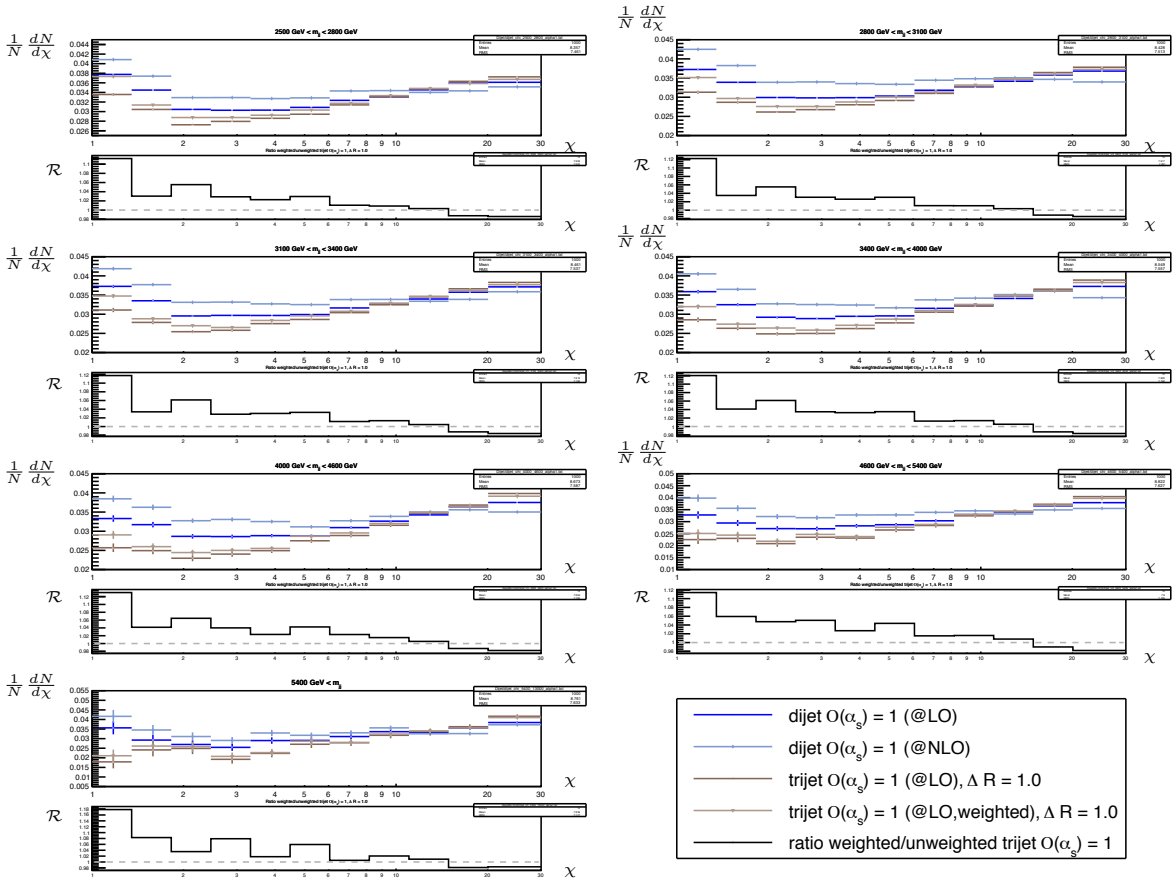

Figure 5.16: Normalised angular distributions for the dijet, NLO corrected dijet, trijet, and weighted trijet topology. The bottom panel displays the ratio of weighted to unweighted trijet topology.

As one would expect, the weighted trijet topology (light brown) is a better approximation of the LO dijet topology (blue) as compared to the unweighted trijet topology (brown). That being said, the effect of the correction is not dramatic enough to adequately explain the large gap between the LO (blue) and NLO (light blue) dijet topology. It is worth mentioning that the differences between the weighted and unweighted trijet topologies are more pronounced in the low χ regime ($\rightarrow$ see ratios displayed in the lower panel of Figure 5.16!). This is expected since high p_T jets - corresponding to larger weight factors and thus bigger corrections - are generally found at low χ for a fixed invariant mass.

5.5.3.2 Variation of the Angular Separation ΔR

As previously mentioned (cf. Section 5.3), the minimum angular separation ΔR between two outgoing partons (defined in Equation (5.9)) is an additional parameter in the trijet topology. Naively, one would expect that the trijet distributions gradually approach the NLO corrected dijet topology as the distance is decreased. In fact, this behaviour is precisely what is observed, see Figure 5.17.

The histograms show the dijet and NLO corrected dijet topology together with the highest ($\Delta R = 1.0$) and lowest ($\Delta R = 0.1$) threshold chosen for the minimum angular separation. As can be seen, the trijet topology becomes more and more similar to the NLO corrected dijet topology as the angular separation ΔR is decreased. In fact, the $\Delta R = 0.1$ trijet topology is an overcorrection that actually exceeds both dijet topologies.

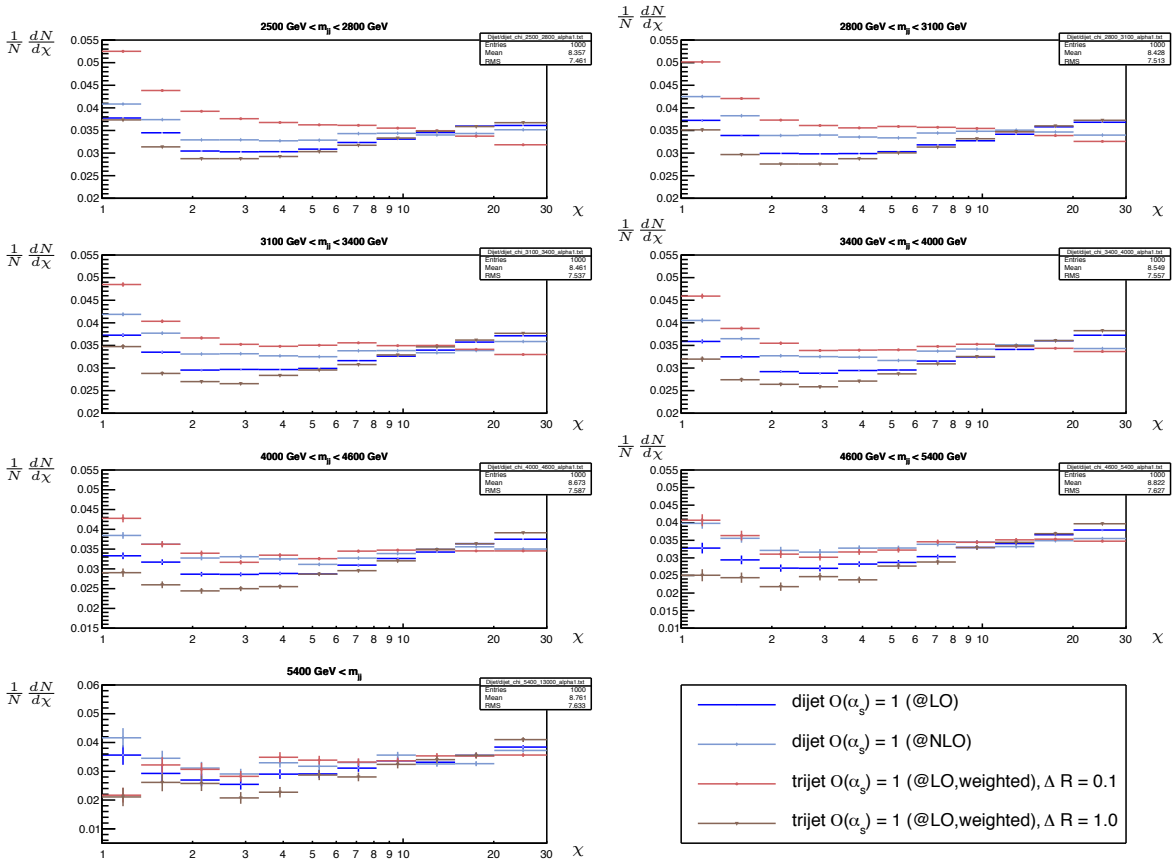

Figure 5.17: Normalised angular distributions for the dijet, NLO corrected dijet, weighted trijet with $\Delta R = 1.0$ and weighted trijet with $\Delta R = 0.1$ topology.

Chapter 6

Conclusions

The ATLAS experiment at the CERN **L**arge **H**adron **C**ollider is searching for new phenomena indicative of BSM physics. Search signatures comprising two jets in the final state are so far not well constrained in the regime of low invariant masses and small vector couplings. This search domain is targeted by the ATLAS dijet **T**rigger **L**evel **A**nalysis.

In the first part of this thesis, a software-based 20 GeV **H**igh **L**evel **T**rigger cut placed on the jet transverse momentum has been implemented in the ATLAS dijet **T**rigger **L**evel **A**nalysis to reduce the average event size from 30 kB/s to 10 kB/s. After tests in cosmic runs showed positive results, the threshold was included as part of the `TrigHLTDSSelector` class and operated successfully during the 2016 data taking period of Run 2 of the LHC. Thanks to the trigger cut, a higher rate of events can be recorded, thus allowing for a significant increase in the sensitivity of low mass dijet searches that were previously limited by the finite trigger bandwidth. To complement searches in the invariant mass spectrum, dijet angular distributions are examined for deviations from the partonic cross sections predicted by QCD. In both cases, the SM background expectation has to be modelled with very high precision in order to be able to identify anomalies in the data. This was the main objective of the second part of this thesis. In particular, angular distributions and kinematic variables have been examined using the MC event generator `PYTHIA 8.219`. Dijet event topologies were studied with and without the production of an additional associated jet (trijet topology) arising from ISR or FSR processes, and were shown to produce sensible results in both cases. Dijet topologies without an additional jet were corrected up to NLO using k-factors derived from `NLOJET++`. Trijet topologies were corrected for differences in the scale of the strong coupling associated with soft emissions using a reweighting procedure and were shown to approach the dijet topology in the limit of small minimum angular separations between two jets.

In future works, one could overlay the results that were obtained with real data collected by the ATLAS detector. Especially in the context of the trijet topology, which has not been considered in previous MC studies, this could possibly give rise to new conclusions.

Bibliography

[1] J. Ellis. *TikZ-Feynman: Feynman diagrams with TikZ*. Number arXiv:1601.05437 [hep-ph]. 2016. doi:10.1016/j.cpc.2016.08.019.

[2] F. Halzen, A. Martin. *Quarks and Leptons: An Introductory Course in Modern Particle Physics*. Wiley, 1984. ISBN 978-0-471-88741-6.

[3] D. Griffiths. *Introduction to Elementary Particles*. Second Edition, Wiley, 2008. ISBN 978-3-527-40601-2. doi:10.1002/9783527618460.

[4] M. Robinson. *Symmetry and the Standard Model: Mathematics and Particle Physics*. Springer, 2011. ISBN 978-1-4419-8266-7. doi:10.1007/978-1-4419-8267-4.

[5] G. Bertone, D. Hooper. *A History of Dark Matter*. Number FERMILAB-PUB-16-157-A. 2016.

[6] B. Novosyadlyj, V. Pelykh, Y. Shtanov, A. Zhuk. *Dark Energy: Observational Evidence and Theoretical Models*. Academperiodyka, 2013. ISBN 978-966-360-240-0. url: https://inspirehep.net/record/1344979/files/arXiv:1502.04177.pdf.

[7] M. Chala, F. Kahlhoefer, M. McCullough, G. Nardini, K. Schmidt-Hoberg. *Constraining Dark Sectors with Monojets and Dijets*. Number arXiv:1503.05916 [hep-ph]. 2015. doi:10.1007/JHEP07(2015)089.

[8] T.Sjöstrand et al. *An Introduction to PYTHIA 8.2*, Volume **191**. 2015. doi:10.1016/j.cpc.2015.01.024.

[9] T. Sjöstrand, S. Mrenna, P. Skands. *PYTHIA 6.4 Physics and Manual*, Volume **05**. 2006. doi:10.1088/1126-6708/2006/05/026.

[10] S. Murk. *High-Mass Dilepton Resonances: Search for grand-unified Z' with the ATLAS detector*. BSc Thesis, Friedrich-Alexander-Universität Erlangen-Nürnberg & The University of British Columbia (Vancouver), 2015.

[11] A. Purcell. *Go on a particle quest at the first CERN webfest. Le premier webfest du CERN se lance à la conquête des particules*. BUL-NA-2012-269, Available on the CERN Document Server at https://cds.cern.ch/record/1473657 (01.12.2016), 2012.

[12] M. Chaichian, I. Merches, A. Tureanu. *Mechanics: An Intensive Course*. Springer, 2012. ISBN 978-3-642-16390-6. doi:10.1007/978-3-642-17234-2.

[13] H. Jones. *Groups, Representations and Physics*. Taylor & Francis Group, 1998. ISBN 978-0-7503-0504-4.

[14] S. Viel. *Search for new neutral high-mass resonances decaying into muon pairs with the ATLAS detector*. PhD Thesis, The University of British Columbia (Vancouver), 2014.

[15] J. Baez. *Hypercharge and Weak Isospin*. 2003.

[16] J. Baez, J. Huerta. *The Algebra of Grand Unified Theories*. 2010.

[17] UA1 Collaboration. *Experimental observation of lepton pairs of invariant mass around 95 GeV/c^2 at the CERN SPS collider*, Volume **126**. 1983.

[18] J. Beringer et al. (Particle Data Group). *Review of Particle Physics*, Volume **86**. American Physical Society, 2012. doi:10.1103/PhysRevD.86.010001.

[19] A. Pich. *The Standard Model of Electroweak Interactions*. 2012.

[20] J. Alison. *The Road to Discovery: Detector Alignment, Electron Identification, Particle Misidentification, WW Physics, and the Discovery of the Higgs Boson*. Springer, 2015. ISBN 978-3-319-10344-0. doi:10.1007/978-3-319-10344-0.

[21] ATLAS Collaboration. *Observation of a new particle in the search for the Standard Model Higgs boson with the ATLAS detector at the LHC*, Volume **B716**. 2012. doi:10.1016/j.physletb.2012.08.020.

[22] CMS Collaboration. *Observation of a new boson at a mass of 125 GeV with the CMS experiment at the LHC*, Volume **B716**. 2012. doi:10.1016/j.physletb.2012.08.021.

[23] L. Randall, R. Sundrum. *Large Mass Hierarchy from a Small Extra Dimension*, Volume **83**, 3370. 1999.

[24] LHCb Collaboration. *Observation of the resonant character of the $Z(4430)^-$ state*. Number LHCB-PAPER-2014-014. 2014. doi:10.1103/PhysRevLett.112.222002.

[25] LHCb Collaboration. *Observation of $J/\psi\phi$ structures consistent with exotic states from amplitude analysis of $B^+ \to J/\psi\phi K^+$ decays*. Number LHCB-PAPER-2016-018. 2016.

[26] LHCb Collaboration. *Observation of $J/\psi p$ Resonances Consistent with Pentaquark States in $\Lambda_b^0 \to J/\psi K^- p$ Decays*. Number LHCB-PAPER-2015-029. 2015. doi:10.1103/PhysRevLett.115.072001.

[27] H. L. Anderson, E. Fermi, E. A. Long, D. E. Nagle. *Total Cross Sections of Positive Pions in Hydrogen*, Volume **85**. American Physical Society, 1952. doi:10.1103/PhysRev.85.936. url: http://link.aps.org/doi/10.1103/PhysRev.85.936.

[28] D. E. Nagle. *The Delta: The first Pion Nucleon Resonance, its Discovery and Applications*. Number LALP-84-27. 1984.

[29] F. Strocchi. *An Introduction to the Mathematical Structure of Quantum Mechanics*. World Scientific, 2008. ISBN 978-981-283-522-2. doi:10.1142/7038.

[30] M. Botje. *Lecture notes Particle Physics II: Quantum Chromo Dynamics: 6. Asymptotic Freedom*. 2013.

[31] ATLAS Collaboration. *The ATLAS Experiment at the CERN Large Hadron Collider*, Volume **3**. 2008. doi:10.1088/1748-0221/3/08/S08003.

[32] ATLAS Collaboration. *The ATLAS Experiment at the CERN Large Hadron Collider*, Volume 1: LHC Machine, ALICE and ATLAS of *The CERN Large Hadron Collider: Accelerator and Experiments*. CERN, Geneva, 2009.

[33] R. Bruce et al. *LHC Run 2: Results and Challenges*. Number CERN-ACC-2016-0103. 2016. url: https://cds.cern.ch/record/2201447.

[34] P. Bogdan, K. Rith, C. Scholz, F. Zetsche, W. Rodejohann. *Particles and Nuclei: An Introduction to the Physical Concepts*. Seventh Edition, Springer, 2015. ISBN 978-3-662-46321-5. doi:10.1007/978-3-662-46321-5.

[35] ATLAS Collaboration. *ATLAS Data Summary: 2016 - pp at 13 TeV*. Accessible at https://atlas.web.cern.ch/Atlas/GROUPS/DATAPREPARATION/DataSummary/2016/records.py (01.12.2016), 2016.

[36] CMS Collaboration. *The CMS experiment at the CERN LHC*, Volume **3**. 2008. doi:10.1088/1748-0221/3/08/S08004.

[37] J. Pequenao, P. Schaffner. *A computer generated image representing how ATLAS detects particles*. Available on the CERN Document Server at https://cds.cern.ch/record/1505342 (01.12.2016), 2013.

[38] M. Schott, M. Dunford. *Review of single vector boson production in pp collisions at* $\sqrt{s} = 7$ *TeV*, Volume **74**. 2014. doi:10.1140/epjc/s10052-014-2916-1.

[39] H. M. M. Mansour, N. Bakhet. *Search for High Energy Electrons from New Neutral Massive Gauge Boson Decay in the CMS Detector at the LHC Using Monte Carlo Simulation*. 2013. doi:http://dx.doi.org/10.4236/ojm.2013.32007.

[40] C. Fabjan, F. Gianotti. *Calorimetry for Particle Physics*, Volume CERN-EP-2003-075. 2003.

[41] P. Krieger. *ATLAS Calorimetry at the Large Hadron Collider*. Invited Talk, Western Regional Nuclear and Particle Physics Conference at Lake Louise, 2004.

[42] P. Puzo. *ATLAS calorimetry*, Volume Section A494. 2002.

[43] ATLAS Collaboration. *ATLAS Detector and Physics Performance: Technical Design Report*. 1999.

[44] P. Czodrowski. *The ATLAS Trigger System: Ready for Run 2*, Volume EPS-HEP2015. 2015.

[45] S. Prince. *The updated ATLAS Jet Trigger for the LHC Run II*. 2015. url: https://inspirehep.net/record/1402596/files/arXiv:1511.00972.pdf.

[46] N. Anjos. *The ATLAS Jet Trigger for LHC Run 2*. Number ATL-DAQ-PROC-2015-034. 2015.

[47] CDF Collaboration. *Search for new particles decaying to dijets at CDF*, Volume **D55**. 1997. doi:10.1103/PhysRevD.55.R5263.

[48] ATLAS Collaboration. *Search for light dijet resonances with the ATLAS detector using a Trigger-Level Analysis in LHC pp collisions at* $\sqrt{s} = 13$ *TeV*. Number ATLAS-CONF-2016-030. 2016. url: https://cds.cern.ch/record/2161135.

[49] W. Lampl et al. *Calorimeter Clustering Algorithms: Description and Performance*. Number ATL-LARG-PUB-2008-002. 2008.

[50] L. Bryngemark. *Search for new phenomena in dijet angular distributions at* $\sqrt{s} = 8$ *and 13 TeV*. PhD Thesis, Lund University, 2016.

[51] J. J. Goodson. *Search for Supersymmetry in States with Large Missing Transverse Momentum and Three Leptons including a Z-Boson*. PhD Thesis, Stony Brook University, 2012.

[52] M. Cacciari, G. P. Salam, G. Soyez. *The Anti-k_t jet clustering algorithm*, Volume 04. 2008. doi:10.1088/1126-6708/2008/04/063.

[53] ATLAS Collaboration. *ATLAS Trigger Operation Public Results*. Technical report, 2016. url: https://twiki.cern.ch/twiki/bin/view/AtlasPublic/TriggerOperationPublicResults#2016_pp_at_13_TeV.

[54] ATLAS Collaboration. *Data Scouting in ATLAS: Trigger, Tier0 and Analysis*. Number ATL-COM-GEN-2014-010. 2014. url: https://cds.cern.ch/record/1957173.

[55] T. Sjöstrand. *Monte Carlo Event Generation for LHC*. Number CERN-TH-6275-91. 1991.

[56] M. Seymour, M. Marx. *Monte Carlo Event Generators*. Number MCNET-13-05. 2013. doi:10.1007/978-3-319-05362-2_8. url: https://inspirehep.net/record/1229804/files/arXiv:1304.6677.pdf.

[57] P. Nason, P. Z. Skands (Particle Data Group). *Review of Particle Physics: 40. Monte Carlo Event Generators*, Volume **86**. American Physical Society, 2013. doi:10.1103/PhysRevD.86.010001.

[58] S. Höche. *Introduction to parton-shower event generators*. Number SLAC-PUB-16160. 2014. url: https://inspirehep.net/record/1328513/files/arXiv:1411.4085.pdf.

[59] P. Nason. *A New method for combining NLO QCD with shower Monte Carlo algorithms*, Volume **11**. 2004. doi:10.1088/1126-6708/2004/11/040.

[60] S. Frixione, P. Nason, C. Oleari. *Matching NLO QCD computations with Parton Shower simulations: the POWHEG method*, Volume **11**. 2007. doi:10.1088/1126-6708/2007/11/070.

[61] S. Alioli, P. Nason, C. Oleari, E. Re. *A general framework for implementing NLO calculations in shower Monte Carlo programs: the POWHEG BOX*, Volume **06**. 2010. doi:10.1007/JHEP06(2010)043.

[62] GEANT4 Collaboration. *GEANT4: A Simulation toolkit*, Volume **A506**. 2003. doi:10.1016/S0168-9002(03)01368-8.

[63] GEANT4 Collaboration. *Geant4 developments and applications*, Volume **53**. 2006. doi:10.1109/TNS.2006.869826.

[64] GEANT4 Collaboration. *Recent Developments in Geant4*, Volume **A835**. 2016. doi:10.1016/j.nima.2016.06.125.

[65] B. Andersson, G. Gustafson, G. Ingelman, T. Sjöstrand. *Parton Fragmentation and String Dynamics*, Volume **97**. 1983. doi:10.1016/0370-1573(83)90080-7.

[66] A. D. Martin, W. J. Stirling, R. S. Throne, G. Watt. *Parton distribution functions for the LHC*, Volume **C63**. 2009. doi:10.1140/epjc/s10052-009-1072-5.

[67] T. Sjöstrand. *PYTHIA 8 online manual*. Accessible at http://home.thep.lu.se/~torbjorn/pythia81html/Welcome.html (01.12.2016), 2016.

[68] ATLAS Collaboration. *Search for new phenomena in dijet mass and angular distributions from pp collisions at* $\sqrt{s} = 13$ GeV *with the ATLAS detector*, Volume **B754**. 2016. doi:10.1016/j.physletb.2016.01.032.

[69] J. B. Hartle. *Gravity: An Introduction to Einstein's General Relativity*. Pearson, 2003. ISBN 978-0805386622.

[70] E. Daw. *PHY 206 Special Relativity: Lecture 7: Rapidity and Pseudorapidity*. 2012.

[71] N. Boelaert. *Dijet angular distributions in proton-proton collisions at $\sqrt{s}$ = 7 TeV and $\sqrt{s}$ = 14 TeV*. PhD Thesis, Lund University, 2010.

[72] CMS Collaboration. *Measurement of Triple-Differential Dijet Cross Sections at $\sqrt{s} = 8$ TeV with the CMS Detector and Constraints on Parton Distribution Functions*. Technical Report CMS-PAS-SMP-16-011, 2016. url: https://cds.cern.ch/record/2235163.

[73] S. Catani, M. H. Seymour. *A General algorithm for calculating jet cross-sections in NLO QCD*, Volume **B485**. 1997. doi:10.1016/S0550-3213(96)00589-5.

[74] Z. Nagy. *Three jet cross-sections in hadron hadron collisions at next-to-leading order*, Volume **88**. 2002. doi:10.1103/PhysRevLett.88.122003.

[75] M. Cacciari, J. Rojo, G. P. Salam, G. Soyez. *Quantifying the performance of jet definitions for kinematic reconstruction at the LHC*, Volume **12**. 2008. doi:10.1088/1126-6708/2008/12/032.

Appendices

Appendix A

Additional Distributions at Different Running Orders $\mathcal{O}(\alpha_s)$

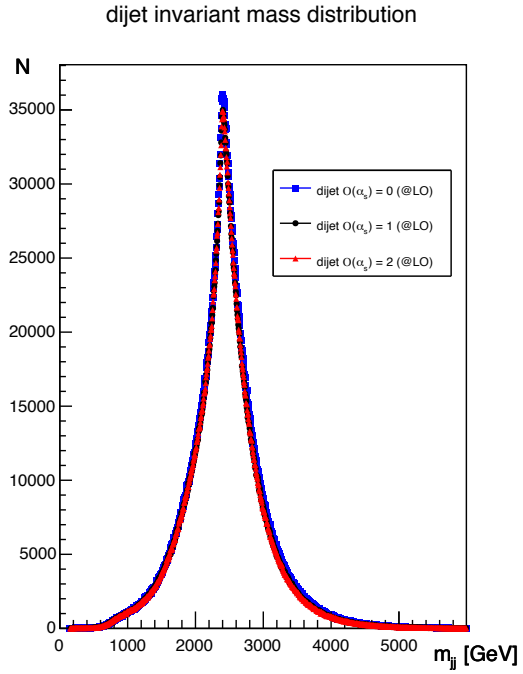

Figure A.1: Dijet invariant mass distribution for three different running orders $\mathcal{O}(\alpha_s) \in \{0, 1, 2\}$ of the strong coupling constant α_s.

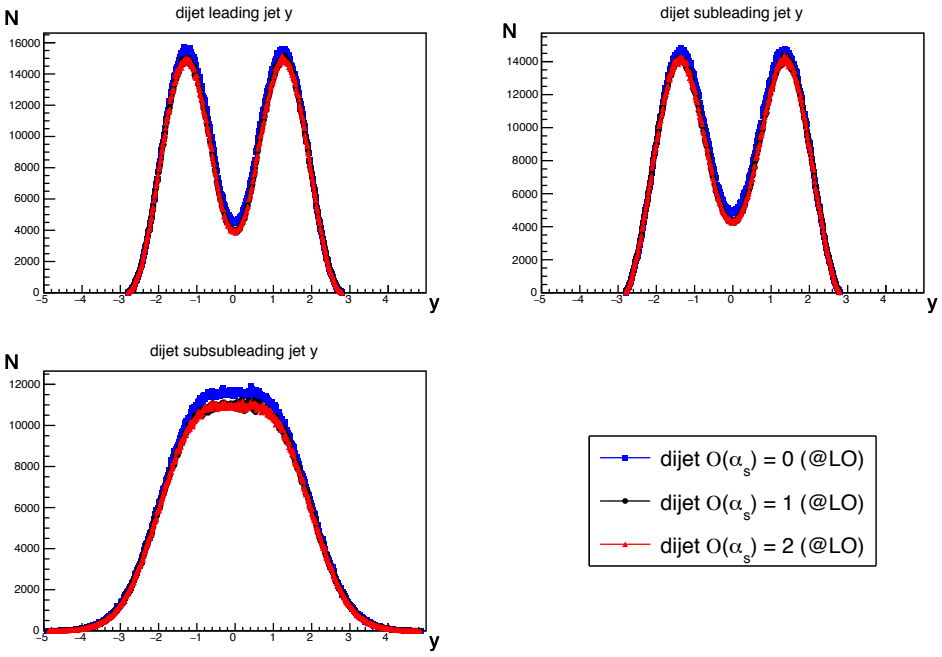

Figure A.2: Rapidity distributions of the leading, subleading and subsubleading jet for three different running orders $\mathcal{O}(\alpha_s) \in \{0, 1, 2\}$ of the strong coupling constant α_s in the dijet event topology.

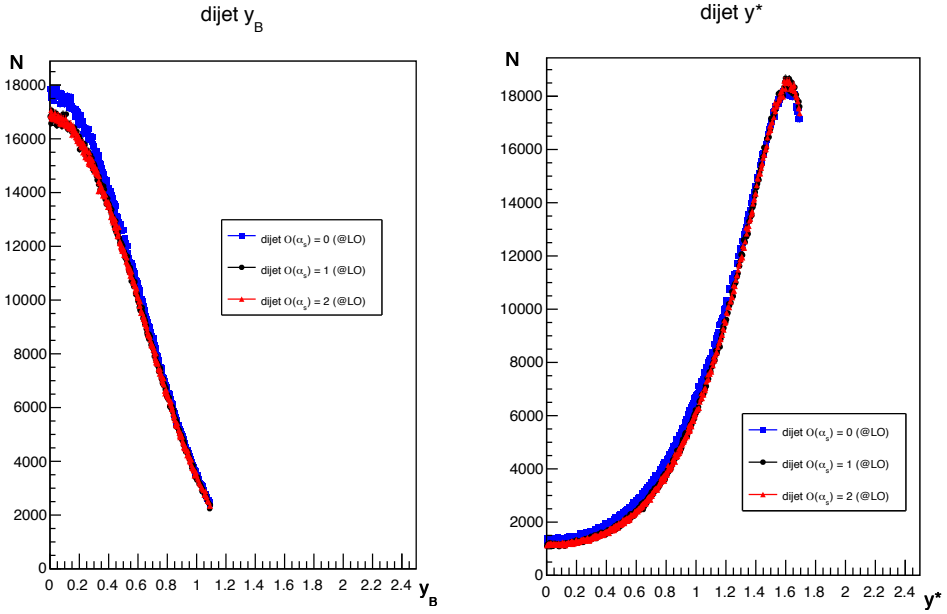

Figure A.3: Angular variables y_B (left) and $y^\star$ (right) for three different running orders $\mathcal{O}(\alpha_s) \in \{0, 1, 2\}$ of the strong coupling constant α_s in the dijet event topology.